NAVAL POSTGRADUATE SCHOOL
Monterey, California

THESIS

STUDY OF PROCESSING AND MICROSTRUCTURE OF A SUPERPLASTIC 5083 ALUMINUM ALLOY

by

Tracy Allen Maestas

March 2002

Thesis Advisor: Terry R. McNelley

Approved for public release; distribution is unlimited

THIS PAGE INTENTIONALLY LEFT BLANK

REPORT DOCUMENTATION PAGE			*Form Approved OMB No. 0704-0188*
Public reporting burden for this collection of information is estimated to average 1 hour per response, including the time for reviewing instruction, searching existing data sources, gathering and maintaining the data needed, and completing and reviewing the collection of information. Send comments regarding this burden estimate or any other aspect of this collection of information, including suggestions for reducing this burden, to Washington headquarters Services, Directorate for Information Operations and Reports, 1215 Jefferson Davis Highway, Suite 1204, Arlington, VA 22202-4302, and to the Office of Management and Budget, Paperwork Reduction Project (0704-0188) Washington DC 20503.			
1. AGENCY USE ONLY *(Leave blank)*	**2. REPORT DATE** March 2002	**3. REPORT TYPE AND DATES COVERED** Master's Thesis	
4. TITLE AND SUBTITLE: Title (Mix case letters) Study of Processing and Microstructure of a Superplastic 5083 Aluminum Alloy			**5. FUNDING NUMBERS**
6. AUTHOR(S) Maestas, Tracy Allen			
7. PERFORMING ORGANIZATION NAME(S) AND ADDRESS(ES) Naval Postgraduate School Monterey, CA 93943-5000			**8. PERFORMING ORGANIZATION REPORT NUMBER**
9. SPONSORING /MONITORING AGENCY NAME(S) AND ADDRESS(ES) General Motors Corp., Research and Development Center, Warren, MI (Dr. Paul E. Krajewski, Technical Program Monitor), under subcontract with Univ. of Texas-Austin (Prof. Eric Taleff)			**10. SPONSORING/MONITORING AGENCY REPORT NUMBER**
11. SUPPLEMENTARY NOTES The views expressed in this thesis are those of the author and do not reflect the official policy or position of the Department of Defense or the U.S. Government.			
12a. DISTRIBUTION / AVAILABILITY STATEMENT Approved for public release; distribution is unlimited			**12b. DISTRIBUTION CODE**
13. ABSTRACT *(maximum 200 words)* Orientation Imaging Microscopy (OIM) methods were applied to the analysis of the microstructure and microtexture as well as the deformation and failure modes of superplastic AA5083 aluminum alloys. Annealing of a cold-rolled AA5083 material at 450ºC resulted in the formation of equiaxed grains approximately 7μm – 8μm in size. Random grain-to-grain misorientations were consistent with particle-stimulated nucleation of recrystallization during processing for superplasticity. Such a microstructure is necessary for superplasticity but mechanical property data indicated only moderate ductility and failure by cavity formation and linkage. This investigation then employed OIM methods to identify the misorientations of boundaries prone to cavitation and determine the role of such boundaries in failure of these materials during elevated temperature deformation.			
14. SUBJECT TERMS Orientation Imaging Microscopy, Superplasticity, Recrystallization, Deformation Mechanism, Grain Boundary Sliding, Dislocation Creep, Cavitation.			**15. NUMBER OF PAGES** 77
			16. PRICE CODE
17. SECURITY CLASSIFICATION OF REPORT Unclassified	**18. SECURITY CLASSIFICATION OF THIS PAGE** Unclassified	**19. SECURITY CLASSIFICATION OF ABSTRACT** Unclassified	**20. LIMITATION OF ABSTRACT** UL

THIS PAGE INTENTIONALLY LEFT BLANK

Approved for public release; distribution is unlimited

STUDY OF PROCESSING AND MICROSTRUCTURE OF A SUPERPLASTIC 5083 ALUMINUM ALLOY

Tracy A. Maestas
Lieutenant, United States Navy
Undergraduate (B.S.), University of Utah, 1995

Submitted in partial fulfillment of the
requirements for the degree of

MASTER OF SCIENCE IN MECHANICAL ENGINEERING

from the

NAVAL POSTGRADUATE SCHOOL
March 2002

Author: Tracy A. Maestas

Approved by: Terry R. McNelley
                     Thesis Advisor

                     Terry R. McNelley
                     Chairman, Department of Mechanical Engineering

THIS PAGE INTENTIONALLY LEFT BLANK

ABSTRACT

Orientation Imaging Microscopy (OIM) methods were applied to the analysis of the microstructure and microtexture as well as the deformation and failure modes of superplastic AA5083 aluminum alloys. Annealing of a cold-rolled AA5083 material at 450ºC resulted in the formation of equiaxed grains approximately 7μm – 8μm in size. Random grain-to-grain misorientations were consistent with particle-stimulated nucleation of recrystallization during processing for superplasticity. Such a microstructure is necessary for superplasticity but mechanical property data indicated only moderate ductility and failure by cavity formation and linkage. This investigation then employed OIM methods to identify the misorientations of boundaries prone to cavitation and determine the role of such boundaries in failure of these materials during elevated temperature deformation.

THIS PAGE INTENTIONALLY LEFT BLANK

TABLE OF CONTENTS

THIS PAGE INTENTIONALLY LEFT BLANK

LIST OF FIGURES

THIS PAGE INTENTIONALLY LEFT BLANK

LIST OF TABLES

THIS PAGE INTENTIONALLY LEFT BLANK

ACKNOWLEDGMENTS

THIS PAGE INTENTIONALLY LEFT BLANK

I.   INTRODUCTION

The cost of processing and forming has always been a major consideration in materials selection for structural components. Conventional metal forming dies are very expensive due to the fact that the die material must be very hard and the die construction must be very robust in order to absorb the high energy required to induce the necessary plastic response. Thus, cost savings can be realized by minimizing the work associated with traditional forming processes.

Superplastic forming offers an alternative to traditional sheet forming techniques because, unlike closed-die pressing, superplastic forming requires minimal work input. However, superplastic forming of aluminum requires heating to high temperatures (generally $\geq 425°C$) and use of slow strain rates (1×10^{-4} to 1×10^{-3} s^{-1}) to achieve the exceptional ductility associated with this phenomenon [Ref. 1]. Superplastic forming is typically accomplished by subjecting a heated sheet of superplastic material to a pressure differential in a chamber as illustrated in the schematic in Figure 1. The sheet initially deforms under biaxial tension as a membrane until it comes in contact with the die; the subsequent flow behavior may then become quite complex. The dies needed for superplastic forming do not require the same strength and hardness as those used for sheet forming thus may significantly reduce the costs associated with their fabrication or purchase [Ref. 2]. Because the strain rate must remain low, long forming times result and this tends to offset the benefits of lower energy input.

It is well known that grain-size refinement provides a powerful method for increasing the strain rate for superplastic forming of materials. Additionally, a decrease in grain size, for a given rate of deformation, results in a decrease in flow stress. Thus, only low applied forces are required during superplastic forming, thereby further reducing energy costs and die wear [Ref. 1]. For this reason, grain size refinement is extremely advantageous. Also, as a result of the decrease in flow stress, there is typically an observed increase in tensile ductility under constant strain-rate conditions [Ref. 1]. This provides another compelling reason for grain refinement.

It is also well accepted that in superplastic metals two competing processes govern the failure of these materials. One is related to macroscopic necking and the other is related to microscopic cavitation. During elevated temperature deformation, the rheological behavior of metallic materials may be understood in terms of the relationship

$$\sigma = k\dot{\varepsilon}^m \qquad \text{Equation 1.1}$$

where σ is the flow stress, k is a material constant, $\dot{\varepsilon}$ is the strain rate and m is the strain rate sensitivity coefficient. The value of m typically ranges from 0.1 - 0.5 for many metals and alloys. The fracture profile of many superplastic metals, (with a strain rate sensitivity coefficient, $m \geq 0.33$), typically reveals only diffuse necking. However, it is also found that the formation of cavities at grain boundaries and their subsequent evolution and linkage leads to premature failure of the materials [Ref. 1].

This study follows and expands on previous research conducted on AA5083 alloys [Refs. 3-5] that specifically addressed the issues of grain refinement and elevated temperature deformation mechanisms in these alloys. An analysis of two types of aluminum alloys, processed to achieve a superplastic response, was conducted using Orientation Imaging Microscopy (OIM) to assess the microstructure and microtexture of these materials. This work examined cavitation behavior of the AA5083 materials designated 978901(A25) and 978083(A20) as well as other material studied in previous research [Ref 2]. Additionally, the recrystallization behavior and deformation response of a new material (ARCO AA5083) was examined in the initial phase of this study.
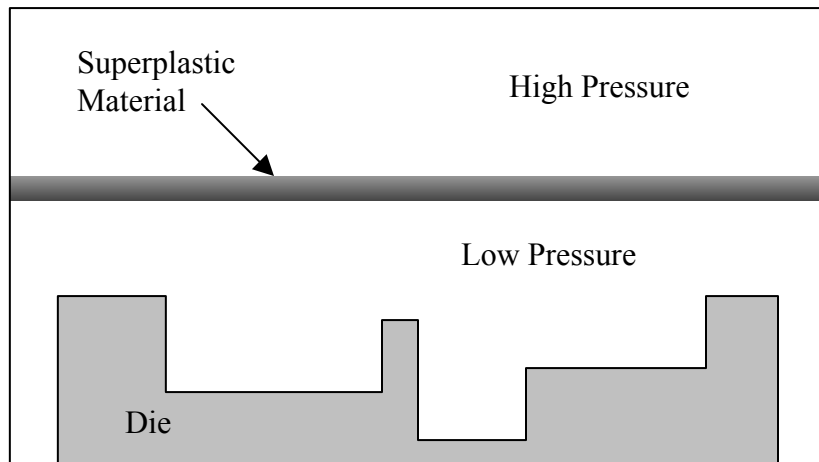
Figure 1.   An illustration of a differential pressure chamber utilized for superplastic forming. (From: [Ref. 2])

THIS PAGE INTENTIONALLY LEFT BLANK

II. BACKGROUND

A. SUPERPLASTIC DEFORMATION MECHANISMS

At the 1991 International Conference on Superplasticity in Advanced Materials (ISCAM-91) held in Osaka, Japan, superplasticity was defined as …"the ability of a polycrystalline material to exhibit, in a generally isotropic manner, very high tensile elongations prior to failure" [Ref. 1]. In certain fine-grained materials very high tensile elongations, perhaps thousands of percent, have been documented and superplastic behavior has been observed in ceramic and composite materials as well as in metals [Ref 1].

Superplastic materials generally exhibit high values of $m \geq 0.33$. Most metals and alloys exhibit typical values of $m \leq 0.2$ although materials, such as hot glass, can exhibit values of $m = 1$, which correspond to Newtonian viscous flow. For a given material a high value of m usually indicates a sufficient resistance to necking to allow a superplastic response to be possible. However, although a high value of m is a necessary condition for superplasticity it is not sufficient to ensure a superplastic response. There is an additional requirement for the material to be resistant to the formation of cavities during tensile elongation to prevent premature failure of the test sample. Therefore, a lower than expected ductility, for a given value of m, may be observed due to development of cavitation damage upon deformation of the material.

It has been observed that the value of m varies as a function of strain rate during tensile elongation at a constant temperature. This variation in m-value has been observed in tensile tests for AA5083 alloys at strain rates varying from 3×10^{-4} s^{-1} to 3×10^{-2} s^{-1} and at a constant temperature of either 500 ºC or 535 ºC [Refs. 2, 5]. This behavior may be attributed to a linear combination of two independent deformation mechanisms contributing to the combined elevated temperature deformation of the material.

The first independently operating deformation mechanism is grain boundary sliding (GBS) accommodated by slip, especially near triple junctions. GBS occurs in a mantle-like region within the region adjacent to the grain boundaries. Plastic

deformation by GBS can be characterized by a strain rate sensitivity coefficient $m = 0.5$. This mechanism usually dominates at low strain rates and high temperatures, $\frac{T}{T_m} \geq 0.5$.

The second independently operating deformation mechanism is dislocation creep (with $m = 0.2 - 0.33$). In turn, dislocation creep involves deformation that is controlled by slip within the grain lattice and involves both glide on slip planes and dislocation climb. The overall rate for dislocation creep can be expressed as [Ref. 1]:

$$\frac{1}{\dot{\varepsilon}_{DIS}} = \frac{1}{\dot{\varepsilon}_G} + \frac{1}{\dot{\varepsilon}_C} \qquad \text{Equation 2.1}$$

where $\dot{\varepsilon}_{DIS}$, $\dot{\varepsilon}_G$ and $\dot{\varepsilon}_C$ represent the total strain rate, the strain rate due to glide and the strain rate due to climb, respectively, for dislocation creep. The smaller strain rate is rate controlling and this accounts for the range in values for the strain rate sensitivity coefficient, m. This mechanism is also characteristic of behavior at $\frac{T}{T_m} \geq 0.3$.

For independent contributions from GBS and dislocation creep, the overall strain rate, $\dot{\varepsilon}$, may be assumed to be given by

$$\dot{\varepsilon} = \dot{\varepsilon}_{DIS} + \dot{\varepsilon}_{GBS} \qquad \text{Equation 2.2}$$

where $\dot{\varepsilon}_{GBS}$ is the strain rate due to GBS. There are various models that have been proposed to describe each of these two independent deformation mechanisms. These models generally assume that each mechanism may be described separately by a relationship similar to that of Equation 1.1, but the appropriate values of k and m for the individual terms are assigned based on the deformation mechanism itself. Furthermore, such models generally incorporate temperature through diffusion coefficients. Such models may be combined [Refs. 1, 5, 6, 7] to yield

$$\frac{\dot{\varepsilon}}{D_L} = \frac{10^{11}}{b^2}\left(\frac{\sigma}{E}\right)^5 + \frac{2 \times 10^9}{\overline{L}^2}\left(\frac{\sigma}{E}\right)^2 \qquad \text{Equation 2.3}$$

where D_L is lattice diffusivity, b is the Burger's vector, $\overline{L}$ is the mean linear intercept grain size, and E is the modulus of elasticity. The first term on the right is the

6

contribution of dislocation creep, which is independent of grain size. The stress exponent of 5 in this term is the reciprocal of the strain rate sensitivity coefficient; thus, $m = 0.2$ if this term dominates. The second term on the right describes GBS, which is grain-size dependent. The stress exponent of 2 equates to $m = 0.5$ and superplastic ductility when this term dominates. Examination of Equation 2.3 reveals that reducing the mean linear intercept grain size, $\overline{L}$, increases the contribution of the second term on the right hand side of Equation 2.3. In turn, this results in an increased range of strain rate, $\dot{\varepsilon}$, over which GBS predominates and wherein $m \cong 0.5$. Thus grain size refinement enhances the range of dominance of the superplastic mechanisms.

B.   PREREQUISITES FOR SUPERPLASTICITY

The prerequisites for superplasticity are well known for aluminum and will be briefly described here. Essentially, the major prerequisites are threefold: 1) a fine-grained microstructure, 2) equiaxed grains, and 3) high angle boundaries.

The requirement for the fine-grained microstructure was discussed in the previous section. In general, the strain rate is inversely proportional to the grain size raised to the second or third power, i.e.,

$$\dot{\varepsilon} \propto d^{-p} \qquad \text{Equation 2.4}$$

where $p = 2$ or 3 [Ref. 1]. A grain size exponent of $p=2$ corresponds to lattice diffusion control of GBS while $p=3$ corresponds to grain boundary diffusion control of GBS. Typical values of grain size for metals should be less than 10 μm [Ref. 1].

Equiaxed grains are needed so that many grain boundaries can experience a shear stress to allow the mechanism of GBS to occur. The requirement of high angle boundaries is to allow grains to slide [Ref. 8]. High angle boundaries can slide while low angle boundaries are inhibited from sliding due to the increased lattice registry between grains. There are additional characteristics that apparently enhance superplasticity. Mobile grain boundaries are known to enhance the superplastic response by allowing

stress concentrations at triple points to relax. Additionally, the grain orientation distribution should be random in nature.

C.   SUMMARY OF PREVIOUS WORK CONDUCTED ON AA5083 ALLOYS

Previous studies on AA5083 aluminum alloys designated lot numbers 978083 and 978901 were conducted at the Naval Postgraduate School in conjunction with mechanical testing conducted at the University of Texas at Austin. The results of the study consisted of microstructure and microtexture data on various stages in the forming process of these superplastic alloys. The as-received condition of these alloys showed an elongated and banded microstructure and a B-type (<112>{110}) deformation texture where the notation refers to <direction parallel to the rolling direction>{plane parallel to the rolling plane}. The materials were annealed for one hour at various temperatures ranging from 425 ºC to 535 ºC in an effort to determine the optimum recrystallization temperature to obtain a fine grain, equiaxed microstructure capable of supporting superplastic deformation (GBS). The results revealed that both materials were fully recrystallized at temperatures $\geq$ 450 ºC and exhibited an area weighted average grain size of 6μm to 8μm.

A microtexture analysis of these materials was then conducted as a function of strain and strain rate during elevated temperature deformation. The results are illustrated in Figure 2 and clearly show the change in microtexture and microstructure as a function of strain rate during tensile deformation at 535 ºC. In the figure, the strength of the microtexture is an indication of the straining conditions. The two dominant deformation mechanisms are clearly delineated, with the GBS regime characterized by a texture randomization and moderate grain growth with a slight elongation in the direction of applied stress. The dislocation creep dominated regime is characterized by a fiber texture formation and a fine (sub) grain structure within elongated grains surrounded by high angle boundaries. The dashed line in Figure 2 is a plot of Equation 2.3 for a mean linear intercept, $\overline{L}$, of 12.7 μm, which is the grain size for material annealed at 535 ºC. The solid line is a curve fit to the data. Equation 2.3 overestimates the deformation rate for

the material but the relationship correctly predicts the stress for the transition from GBS

to dislocation creep (at $\frac{\sigma}{E} \cong 3 \times 10^{-4}$).

Further mechanical testing conducted at the University of Texas at Austin revealed significant ductility differences between the two AA5083 materials, designated 978901 and 978083. OIM analysis revealed no significant differences in the microstructure and microtexture of the two materials and attributed the differences in ductility to cavitation differences [Ref. 2]. Results of this investigation of the 978901 and 978083 materials as well as the ARCO material will be presented in Chapter IV of this thesis.
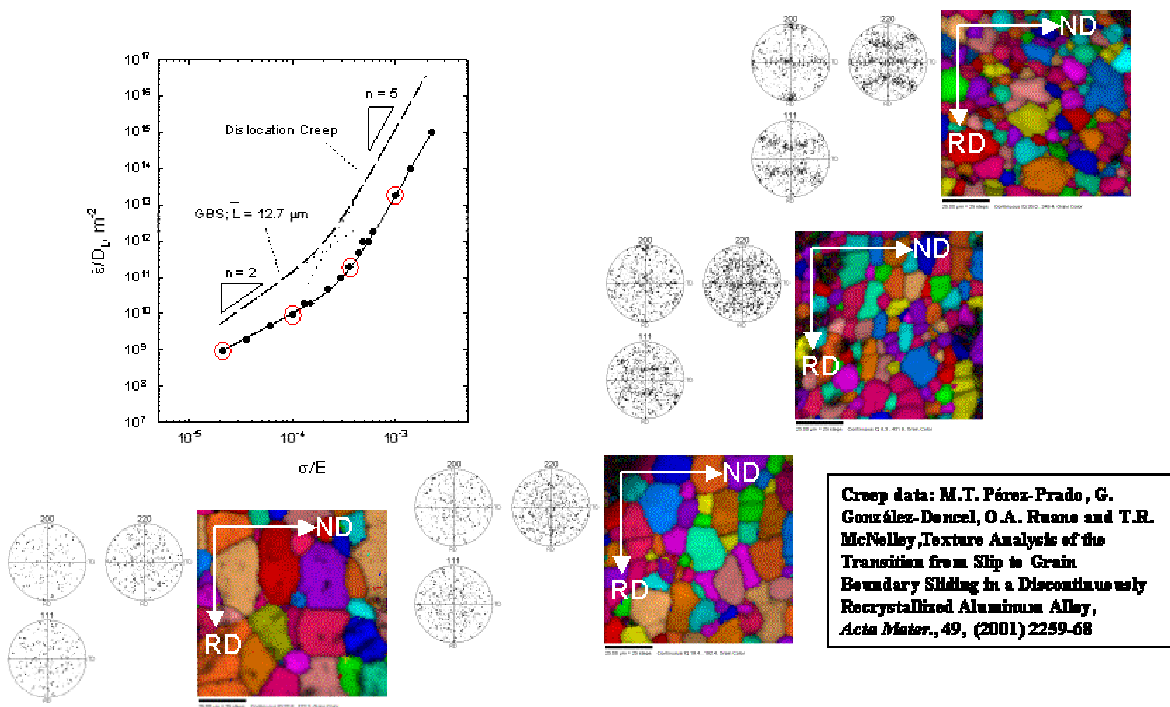
Figure 2.   Results from previous work conducted on AA5083 alloys deformed in tension at a temperature of 535 ºC, illustrating the change in microstructure and microtexture as a function of strain rate. (Courtesy of T.R. McNelley)

III.   EXPERIMENTAL PROCEDURES

A.   OVERVIEW

In this study, AA5083 aluminum-magnesium alloys that had been processed for grain refinement and superplasticity were examined. Specifically, ARCO materials designated, AR12 or AR16, as well as two other materials, designated 978083 and 978901 were studied. All materials were provided by the University of Texas at Austin.

This study was essentially divided into four major phases. In the first phase, an OIM investigation of the ARCO materials was conducted in the as hot rolled condition and following 66% cold reduction (designated AR16) or 76% cold reduction (designated AR12). In the second phase, an OIM investigation of recrystallization in the cold rolled ARCO materials was conducted after anneals at 450 ºC. This was intended to assess the dependence of grain size as a function of prior deformation strain. The annealing times for both the AR16 and AR12 materials were 0.1, 0.2, 0.5 and 1.0 hrs. The third phase involved an OIM investigation of the AR16 material to assess the dislocation creep to GBS mechanism transition during deformation at 450 ºC. Previous work of a similar nature had been conducted at the Naval Postgraduate School, involving AA5083 alloys strained at an elevated temperature of 500 ºC. In the final phase, an OIM investigation was conducted on the 978083 and 978901 materials, strained at 500 ºC, to identify the onset of cavitation and determine its role in the failure of these materials during elevated temperature deformation.

B.   MATERIALS

Samples of the ARCO materials were provided in the form of an as-rolled sheet material. The as hot rolled material was 4.7mm in thickness, while the AR16 and AR12 materials were 1.6 mm and 1.2 mm in thickness respectively. The rolling direction was identified by the surface texture in these materials. Compositions (in wt%) of the ARCO materials are consistent with compositions (in wt%) of the 978083 and 978901 materials

provided in previous work [Ref. 2]. They are included in this table for reference purposes.

Lot No.	Si	Fe	Cu	Mn	Mg	Cr	Zn	Ti	Zr
978083	0.09	0.21	0.04	0.86	4.71	0.10	0.05	0.01	0.00
978901	0.06	0.11	0.01	0.78	4.69	0.06	0.00	0.01	0.00

Table 1.   Chemical composition data for the 978083 and 978901 materials. (From: [Ref 2, 10])

A summary of the thickness and percent cold reduction (% CW) for all the materials analyzed in this study is presented in Table 2.

Lot No	Gauge (mm)	% CW
978083	1.4	74.0
978901	1.6	74.0
ARCO Hot Rolled	4.7	0.0
AR16	1.6	66.0
AR12	1.2	76.0

Table 2.   Final gauge and %CW for each material in the as-rolled condition. (From: University of Texas at Austin).

C.   ANNEALING PROCEDURES

In order to conduct the annealing study, samples were sectioned from the sheet material using a Buehler low-speed saw equipped with a diamond-wafering blade (Series 15 LC Diamond). The sectioning was conducted at a blade speed of 400 rpm with no more than 100 g. load being applied throughout the sectioning process. The samples were sectioned parallel to the rolling direction to facilitate examination of the effects of rolling in the RD-ND plane as illustrated in Figure 3. The annealing for the recrystallization study was conducted in this laboratory. Annealing was conducted at 450ºC for both AR12 and AR16 materials. The annealing times were 0.1, 0.2, 0.5, and 1.0 hrs for both materials. Annealing was conducted using a NEY 2-160 Series 11 laboratory furnace with the sample temperature monitored utilizing two Type-K NiCr-NiAl thermocouples with a Model HH21 Omega Microprocessor Thermometer. A 12.7 mm thick brass plate was placed on the furnace hearth as a heat sink to facilitate a rapid equilibration of the sample temperature. A 31.8 mm x 6.4 mm x (either 1.2 mm or 1.6 mm) sample was placed on the brass plate with the thermocouples on either side of the sample to monitor temperature. Measurements showed that the annealing temperature was reached and stabilized within one minute of placing the samples in the hearth. After the predetermined annealing time was completed, the samples were removed and allowed to cool in air to room temperature.

D   SAMPLE PREPARATION FOR OIM

For OIM of aluminum, the region from which electron backscattered diffraction patterns are formed extends only to a depth of 50 nm below the surface [Ref. 9]. Therefore, sample preparation must be aimed at achieving a smooth, uniform and strain free condition at the surface. Minimizing the damage due to metallographic preparation and preventing surface contamination and oxide formation subsequent to polishing is absolutely necessary. Accordingly, the samples that had been deformed at elevated temperature were sectioned as illustrated in Figure 4. These samples were sectioned

utilizing the procedure and equipment mentioned previously in Chapter 3 Section C. As before, they were sectioned to allow examination of the RD-ND plane. These samples, as well as the AR12 and AR16 samples that were sectioned for annealing previously, were subjected to a mechanical grinding and polishing procedure summarized in Table 3. Initial grinding was conducted utilizing successively finer silicon carbide fixed abrasives. Rotating wheels were used, at low rpm, using minimal downward force for the mechanical grinding steps. Grinding was conducted at each step until evidence of the prior grinding step was removed, whereupon the sample was rotated 90º and the procedure was repeated. The samples were flushed with filtered water between each grinding step. Rotating wheels, at higher rpm, were used for subsequent polishing steps using oil-based diamond suspensions and a final mechanical polishing step was conducted utilizing dilute colloidal silica suspension. The dilution was accomplished using drop wise applications of filtered water while polishing. Dilute dispersions of all abrasives were utilized to prevent saturation of the polishing wheels and subsequent contamination of the sample's surface. Additionally, minimal downward force was used while polishing to prevent displacing the lubricants in the abrasive solutions. Ultrasonic cleaning was conducted between each polishing step for ten minutes in ethanol in an ice bath to prevent recovery or grain growth of the annealed samples.

An electropolishing was conducted as a final preparation step to achieve a distortion free surface and maximize the quality of the diffraction patterns. The electropolishing was conducted utilizing a Buehler Electromet 4 Electro-polisher at a voltage necessary to achieve a current density of 3.8 A/cm^2 for 10 sec. The electrolyte was a 80/20-vol% Perchloric Acid/Ethanol mixture cooled to -25ºC. The samples were rinsed in ethanol and either placed directly in the scanning electron microscope or stored in ethanol to prevent oxidation while awaiting examination.

ND

RD

TD
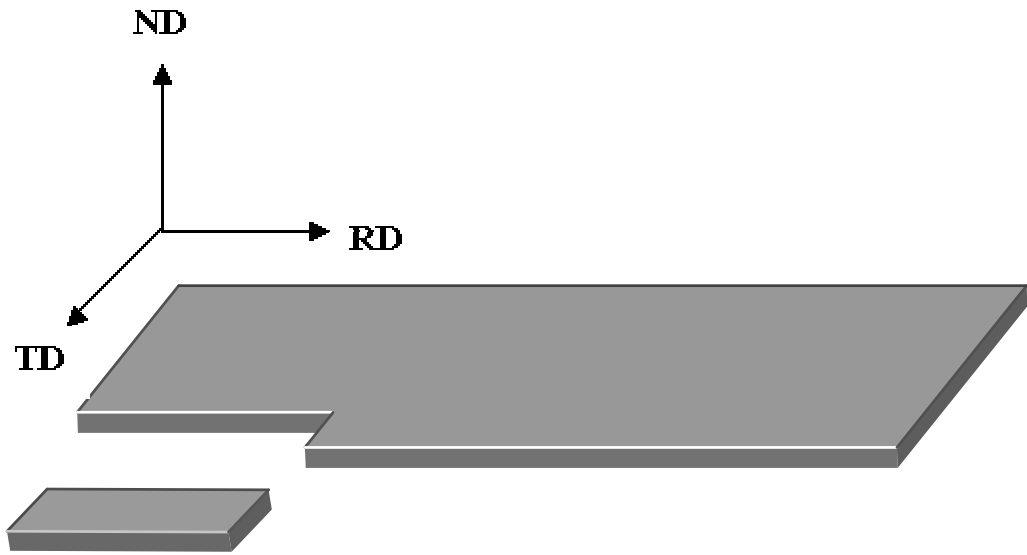
Figure 3.   Schematic of material in as-rolled condition. RD, ND and TD represent rolling direction, normal direction and transverse direction, respectively. The sample was sectioned along RD in order to examine the microstructure on the RD-ND plane

ND

RD

TD

Region Studied
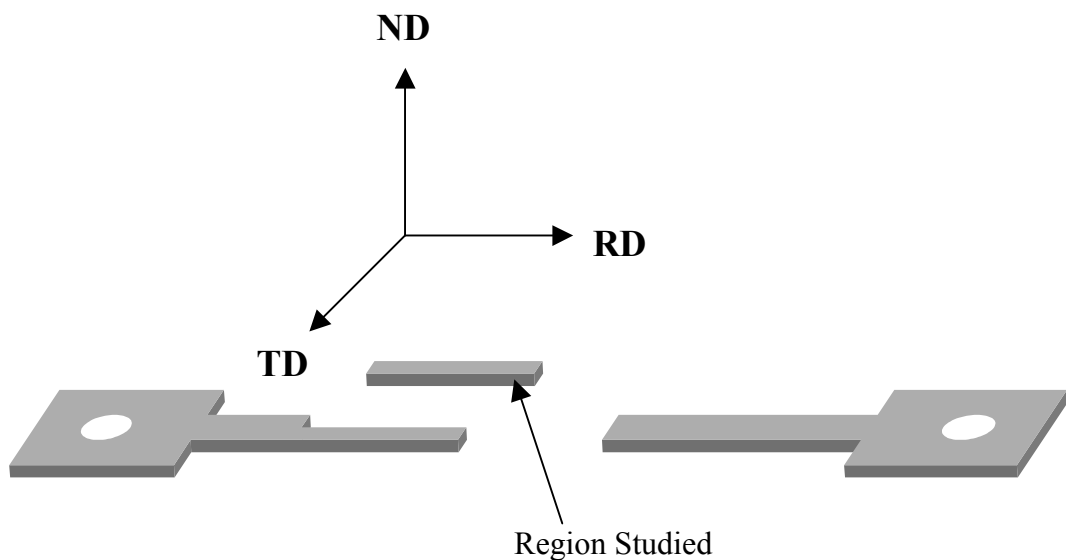
Figure 4.   Schematic of a deformed tensile sample illustrating sectioning for OIM examination. (From: [Ref. 2]).

Step	Abrasive	Time	RPM
1	500 Grit SiC Paper	30 sec	20
2	1000 Grit SiC Paper	30 sec	20
3	2400 Grit SiC Paper	30 sec	20
4	4000 Grit SiC Paper	30 sec	20
5	3 μm Metadi Diamond Suspension	10 min	180
6	1 μm Metadi Diamond Suspension	10 min	180
7	0.05 μm Colloidal Silica	10 min	90

Table 3.   Mechanical Polishing Procedure

D.   ELECTRON BACKSCATTER DIFFRACTION PATTERN COLLECTION

Electron backscatter diffraction patterns were obtained in a TOPCON SM-510 Scanning Electron Microscope (SEM) equipped with a tungsten filament.   The microscope was operated at an accelerating voltage of 20 kV and a beam diameter of 96nm. The polished sample was mounted in the SEM on a specially designed stage that holds the sample at a 70º angle relative to the incident electron beam, enabling Bragg diffraction conditions to be met without rocking the source. When an electron beam strikes a surface inclined in this manner, the electrons penetrate the sample surface and are diffracted to produce distinct patterns based on the local lattice orientation. These patterns appear as multiple intersecting lines, termed Kikuchi bands. These bands represent the reflecting planes in the diffracting crystal volume. The geometrical arrangement of the bands is a function of the orientation of the diffraction crystal lattice [Ref. 9].

The diffracted electrons illuminate a phosphor screen mounted near the sample. A low-light CCD camera is used to collect the image of the Kikuchi patterns from the phosphor screen for indexing by the OIM data collection software. An image-processing algorithm (Hough Transform) is then used to detect the bands in the diffraction pattern. The pattern can than be indexed by comparing the angles between the detected bands to a theoretical look-up table, based on the expected crystal structure. Indexing the pattern allows the crystallographic orientation to be determined for that point. As the beam is moved from point to point, the electron backscatter diffraction pattern will change due to the change in the orientation of the crystal lattice in the diffracting volume [Ref. 9]. The arrangement of the equipment is illustrated in the simplified schematic in Figure 5. The overall outline of image generation is illustrated in Figure 6.

Prior to the collection of data, the user must instruct the software to calibrate reference patterns to the detected Kikuchi patterns from the material. This calibration corrects for distance error caused by slight mounting variations from one sample to the next that would otherwise cause the lines in the reference pattern to be of different length than those generated by the diffraction pattern. When indexing the detected bands, there

17

are generally several possible solutions that can be made to fit the detected bands relative to the reference pattern. Therefore, when indexing the detected bands, a numerical ranking is assigned to each possible solution using a voting scheme based on how closely the proposed reference pattern fits the detected Kikuchi bands. The solution that best fits the detected Kikuchi bands is taken as the orientation of the point and the software records the Euler angles for that pattern. The solution is expressed in terms of the Euler angles φ_1, Φ, and φ_2 (Bunge's definition [Ref. 11]) that describe the rotation necessary to cause the cube axis and sample axes to coincide.

The OIM software also computes two figures of merit for the diffraction data: the confidence index (CI) and the image quality (IQ). The CI is a measure of the certainty that the correct orientation for the data point has been selected. Its value is based on the voting scheme use in ranking proposed solutions and is determined by the equation $CI = \frac{(V_1 - V_2)}{V_{IDEAL}}$ where V_1 is the number of votes for the first solution, V_2 is the number of votes for the second solution, and V_{IDEAL} is the total number of votes for all the proposed solutions. The CI value can range from zero to one and CI values greater than 0.1 correspond to a 95% probability that the Kikuchi pattern has been correctly indexed. However, it should be noted that a CI=0 does not necessarily mean that the point was indexed incorrectly. Such a condition, (CI=0), could exist if $V_1 = V_2$.

The IQ is a measure of the sharpness of a given electron backscatter diffraction pattern. The IQ is a function of many parameters, some of which are the topographic conditions of the sample, brightness of the image sent to the image processor and the strain energy in the sample. For example, an increase in strain energy in the sample, caused by imperfections such as dislocations, or the overlapping and spreading of patterns nearby grain boundaries can produce more diffuse patterns and thus, more poorly defined Kikuchi bands. Therefore, the IQ parameter is useful in obtaining a qualitative description of regions of high strain energy (high dislocation density). Regions of low IQ are also found nearby grain boundaries.

The electron beam provided by a SEM has a typical diameter range of 50 nm to 150 nm. Therefore, the beam only interacts with a very small volume of the sample

relative to typical grain dimensions in engineering materials and so the resulting orientation data represents the local lattice orientation at a point within the grain. If the electron beam is displaced from point to point in a pattern on the surface of a sample, the resulting orientation data may be assembled into a map of orientations of the sample surface. The OIM software displaces the electron beam in a raster pattern across the sample surface. In this investigation, a hexagonal raster pattern was used for all samples. The size of the scan and the step size are user selectable. The system employed in this study was capable of indexing about 3 points per second, or 10,000 points per hour. The region to be scanned is selected on a secondary electron image of the surface. As the surface of the sample is scanned, data for each point is saved in a single line comprising the Euler angles (φ_1, Φ, φ_2), coordinates relative to the origin of the scanned region (x,y), the IQ, and the CI. The set of data lines corresponding to each point in a scanned region on the sample surface is saved as a *.ang file. This file is the source for all subsequent data analysis.
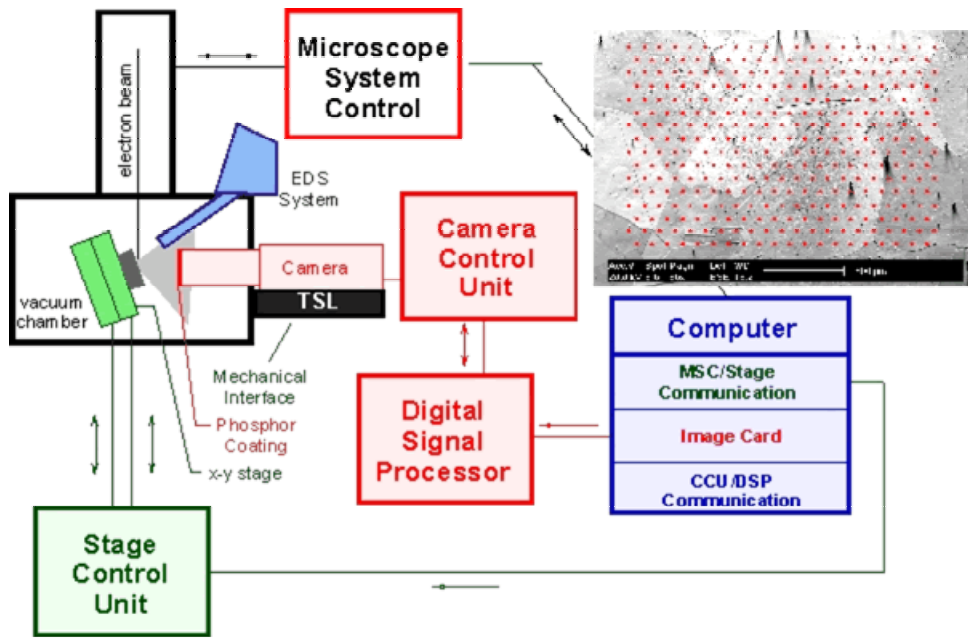
Figure 5.   Schematic illustrating the SEM-OIM equipment setup. The top right image illustrates a typical raster pattern used to obtain a map. (From: TSL-OIM.com)
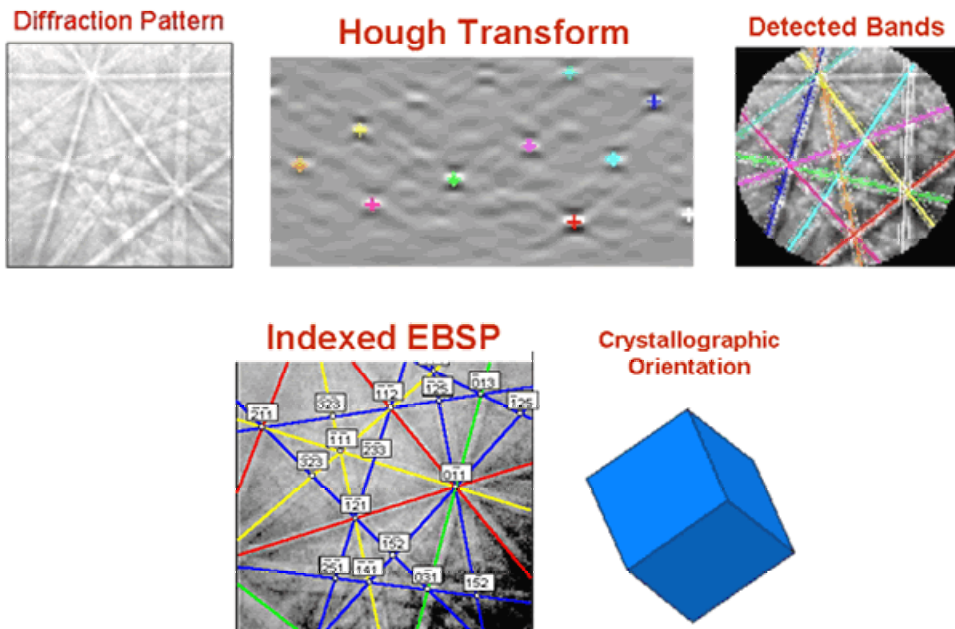
Figure 6.   Schematic illustrating the raw diffraction pattern, Hough Transform, the resulting detected bands and the final indexed EBSP based on the crystallographic orientation shown. (From: TSL-OIM.com)

F.   ELECTRON BACKSCATTER DIFFRACTION PATTERN ANALYSIS

An introduction to electron backscatter diffraction pattern analysis and OIM has been given by Randle [Ref. 9]. In OIM, the orientation data may be assembled into grain maps. The user defines a grain in the OIM system by establishing the grain tolerance angle and the minimum number of points that may define a grain. The grain tolerance angle is defined as the maximum misorientation between two points that are considered to reside in the same grain. Here, misorientation refers to the minimum angle among all crystallographically equivalent rotations necessary to bring adjacent crystal lattices into coincidence. Thus if two adjacent points have a misorientation angle that exceeds that set by the grain tolerance angle, the OIM system assigns each point to separate grains and defines the boundary between the points as a grain boundary, assuming that the number of points that define a grain was set at one. In this study, the number of points that define a grain was set at one, while the grain tolerance angle was taken as $2º$

The OIM analysis software creates a grain map by considering the orientations of all the points in a scan, and applying one of several attributes to develop a "contrast" mechanism. One attribute is the orientation of each of the points, as defined above. In this method, the system assigns a color, at random, to a set of points defined as a grain in accordance with the preceding discussion. The combined effect results in a unique grain color map, an example of which is show in Figure 7. It is important to note that the color assigned is not related to the properties of the grain, and, as such, grains that were assigned the same color may or may not have the same orientation associated with them. The importance of each grain being assigned a separate color is to identify the areas in that same colored area that meet the grain tolerance angle criteria from point to point, thereby defining the grains and grain boundaries. Once the grains have been identified, grain-size data may be calculated by determining the area of each pixel and the number of pixels in each grain. Then, the area average planar grain diameter $\bar{d}$, is calculated by determining the average equivalent diameter of a circle of area equal to the average grain area, i.e.,

$$\bar{d} = \frac{1}{A}\sum_{n=1}^{N} 2\sqrt{\frac{f_A M_n}{\pi}} \qquad \text{Equation 3.1}$$

where N is the number of grains in the grain map and M_n is the number of points in the

nth grain. The function f_A is given by,

$$f_A = \left(\frac{\sqrt{3}}{2}\right)\Delta x^2 \qquad \text{Equation 3.2}$$

where Δx is the beam step size.

Another method to develop a "contrast" mechanism is to generate a grayscale map. In this method, the analysis software assigns a different level of gray proportional to a property that is selected by the operator. For example, an Image Quality (IQ) grayscale map will have regions of high IQ depicted by lighter shades of gray and areas that correspond to lower values of IQ will be assigned darker shades of gray. In this manner, areas of high dislocation density, which would have a correspondingly low value of IQ, would appear darker in an IQ grayscale map. An example of an IQ grayscale map is shown in Figure 8; these data are for the same area as Figure 7. A comparison of Figures 7 and 8 shows that most regions (grains) are similarly identified. However, some fine grains are apparent in Figure 8 and are not seen in Figure 7 due to the use of a 2º minimum grain tolerance in Figure 7.

Additionally, pole figures and misorientation distribution profiles can be directly generated using the orientation data obtained by the collection software. The data obtained in these items can be directly correlated with the grain maps to identify areas of interest by highlighting.

Cleanup procedures in the OIM analysis software were applied to all scans in order to compensate for erroneous data points. While pattern indexing in OIM is generally quite effective in most regions of a sample surface, the system does have difficulty indexing in some circumstances. Regions of low image quality where Kikuchi bands are diffuse, or nearby grain boundaries where patterns from adjacent grains can superimpose are such circumstances. In general, clean-up methods correct for small grains of low CI by incorporating them into larger adjacent grains of high CI. Three

clean-up methods were used for each scan. First, CI Grain Standardization assigned the highest CI for a point within a grain to the entire grain. Then, Neighbor CI Correlation assigned a grain with a confidence index less than 0.1 (95% certainty) to the neighboring grain with the highest CI. Finally, Grain Dilation assigned any leftover grains with a grain size corresponding to one data point to its neighbor with the highest CI.
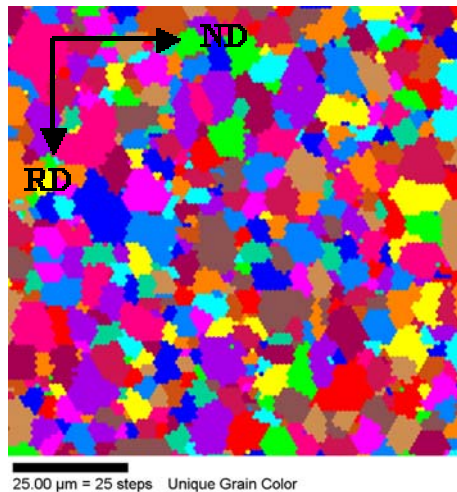
Figure 7. Unique grain color map of a recrystallized material. Each individual grain color is associated with an area wherein the point-to-point misorientation angle is less than the value assigned to the grain tolerance angle parameter.
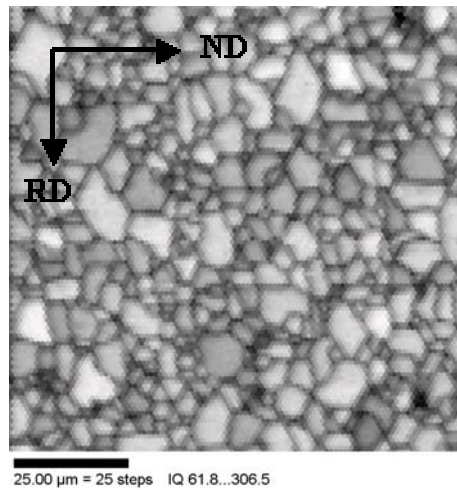
Figure 8. An IQ grayscale grain map of the same area shown in Figure 7. In this type of grain map, the contrast is developed by the varying image quality that is associated with the diffuseness of the diffraction patterns.

IV.   RESULTS AND DISCUSSION

A.   THE MICROSTRUCTURAL ANALYSIS OF THE HOT-BAND AA5083 MATERIAL

An OIM analysis was performed on the ARCO hot band material in the as hot-rolled condition in order to determine the microstructure and microtexture of the material in the first stage of processing for comparison to the subsequent steps. Figure 9 reveals the results of the analysis. Figure 9(a) shows a typical IQ grayscale grain map of the runs conducted on this material. The microstructure revealed in this grain map appears to consist of randomly oriented, equiaxed grains, as well as some grains that are elongated in the RD. Additional analysis of the microstructure revealed the area weighted average grain size for all the runs conducted on this material was 12.8 μm, which is relatively fine. Often, grain sizes in hot rolled aluminum are 30 μm to 50 μm and further investigation is required to determine the reason for this grain size difference.

The results of the microtexture analysis, as revealed by the pole figures shown in Figure 9(b), show a random component and a weak cube (<100>{001}) orientation at this stage of processing. The cube is a recrystallization component. The predominantly random distribution of orientations is reflected in the misorientation distribution plot, Figure 9(c). This plot is essentially similar to a Mackenzie distribution obtained by randomly orientating cubes [Ref. 12]. The combined results suggest that the grain-to-grain misorientations, of the material, are essentially random in nature and are consistent with a material in a recrystallized state.

(a)

(b)
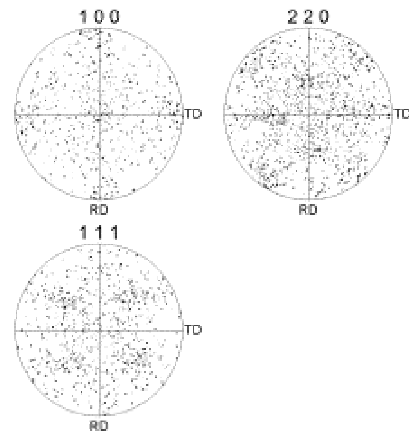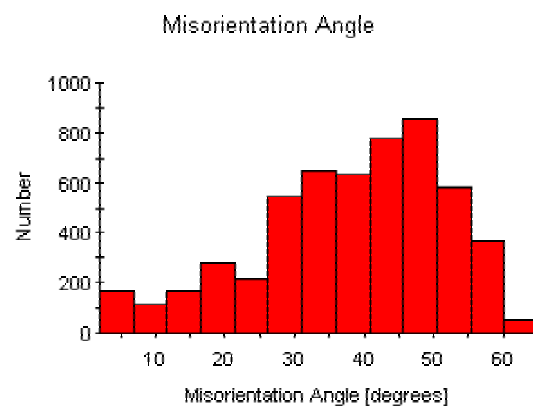
Figure 9.   Microstructure and microtexture data for the ARCO material in the hot-band condition. The relatively fine equiaxed microstructure is evident in the IQ grain map (a). The microtexture is revealed in the pole figures (b) as essentially randomly oriented with a slight deformation texture showing. The grain-to-grain misorientation distribution (c) confirms the pole figure data and additionally reveals the high degree of high angle boundaries associated with the microstructure.

B.   THE COLD ROLLED CONDITION OF THE AA5083 ALUMINUM ALLOYS (AR12 AND AR16)

The OIM analysis of the AR12 and AR16 AA5083 materials revealed a severely deformed microtexture resulting from cold rolling. In Figure 10, an image quality grayscale and unique grain color map of the AR 12 material are superimposed. This image reveals a mixture of a fine (sub) grain structure with highly elongated coarser grains aligned in the rolling direction. The darker regions of the map represent areas of low image quality resulting from a higher dislocation density, which reflects a high strain in the lattice as a result of the cold working. Figure 11 is a similar image, but for the AR16 material. The image is essentially the same in its features; however, the elongated grains appear to be coarser and better defined in the map.

The orientation data for the AR16 material is plotted in Figure 12 in the form of a contour plot in Euler space for a face centered cubic material. The contours were calculated in the OIM software by the smoothing of Gaussian distributions about locations in Euler space of the discrete orientation measurements. The data show a predominant brass (B) texture component. The ideal B orientation is {110}<112>, where the notation refers to {plane parallel to the rolling plane}<direction parallel to the rolling direction>. This component has two crystallographically distinct variants, B1 and B2, which are located at: $\varphi_1 = 35º$, $\Phi = 45º$, $\varphi2 = 0º$, and, $\varphi_1 = 55º$, $\Phi = 90º$, $\varphi2 = 45º$, respectively. These variants are readily distinguished in electron backscatter diffraction analysis and so the relative intensities at the locations for the two variants are not the same if the relative volume of material having each of these orientations differs in the region under investigation [Ref. 2.]. Figure 12 clearly shows the local intensity is greatest at these locations, which is consistent with the B texture.

Using the highlighting feature of the OIM program, the spatial distributions of these orientations can be correlated to the associated IQ grain map. Figure 13 (a) and (b) illustrates this feature. In this figure, the B_1 and B_2 texture components have been highlighted on the pole figures. The associated regions on the IQ map, corresponding to these components, have been highlighted with similar colors as a means to identify them spatially. The use of highlighting clearly shows an alternating B_1 and B_2 banded

structure. The appearance of these bands suggests a deformation-banding model previously seen in severe rolling operations and is consistent with previous studies conducted in this laboratory [Refs. 2, 13].

Additionally, the OIM analysis software was used to highlight the grain interface locations in order to determine the location of the high angle boundaries (defined as a grain-to-grain misorientation of >15º) and low angle boundaries (defined as a grain-to-grain misorientation of 2º - 14º) in comparison to the spatial location of the texture bands. Figure 13 illustrates the results of this analysis, and clearly shows that the bands are separated by high angle boundaries. The low angle boundaries can be associated with a (sub) grain cell structure within the bands. These results are again consistent with previous studies conducted on the AA5083 materials designated 978901 and 978083 [Ref. 2]. The extensive presence of high angle boundaries as shown in Figure (c) coupled with the banded structure in the presence of a large amount of deformation induced strain energy will provide the conditions for recrystallization [Ref. 14].
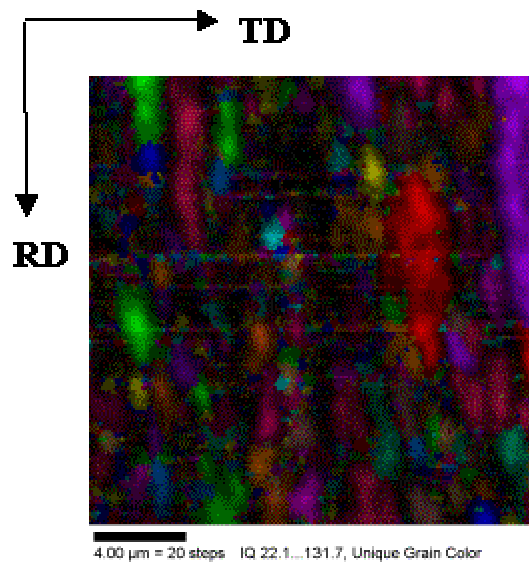
Figure 10. An image quality grayscale unique grain color map of a 20μm x 20μm area of AR12 material in the as-received condition utilizing a 0.2 μm step size. The image reflects a mixture of a fine (sub) grained structure with better-defined, coarser grains elongated in the rolling direction.
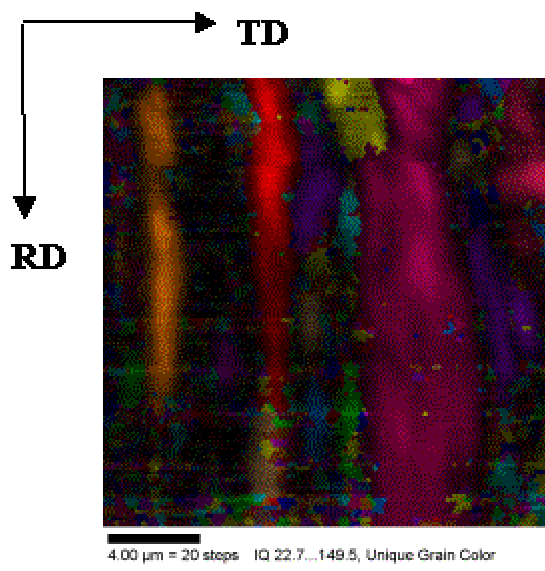
Figure 11. An image quality grayscale unique grain color map of a 20μm x 20μm area of AR16 material in the as-received condition utilizing a 0.2 μm step size. This structure is essentially the same as described in Figure 9, however, the elongated coarser grains appear to be larger in size and better defined.
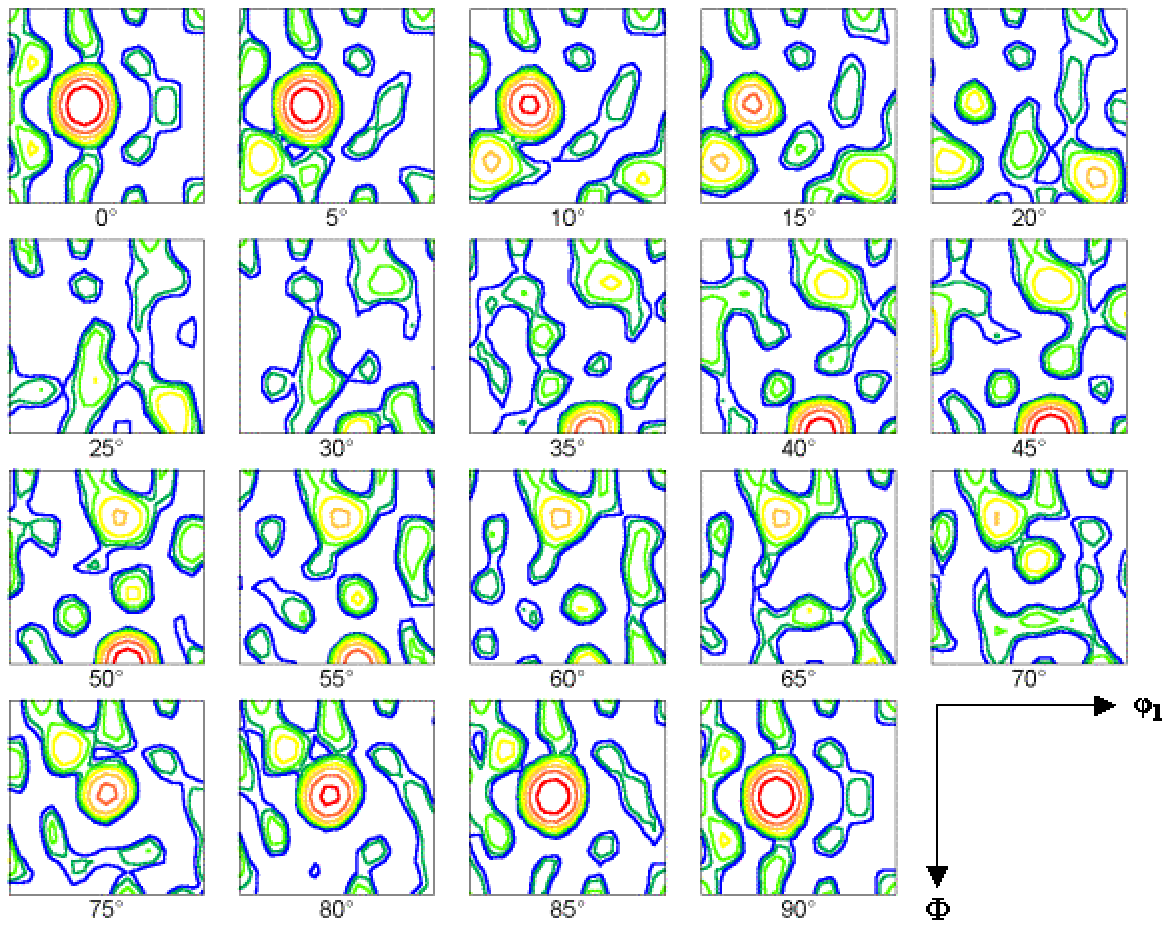
Figure 12. Euler space contour map for the AR16 material revealing distinct B1 and B2 texture components at (φ_1=35º, Φ=45º, φ_2=0º) and (φ_1=55º, Φ=90º, φ_2=45º) respectively. The red lines indicate an increased local intensity at that point described by the Euler angles. The contour plot was constructed by ranging φ_1 and Φ from 0º-90º, with 5º increments, holding φ_2 constant.
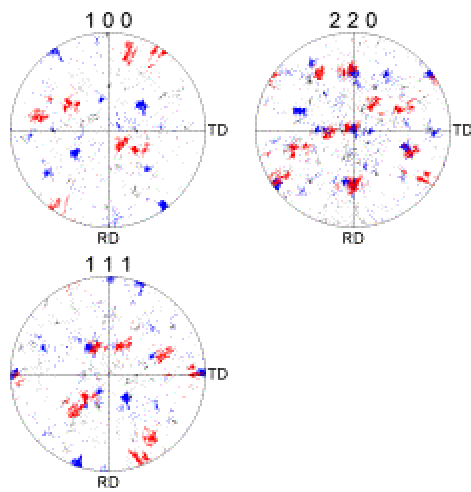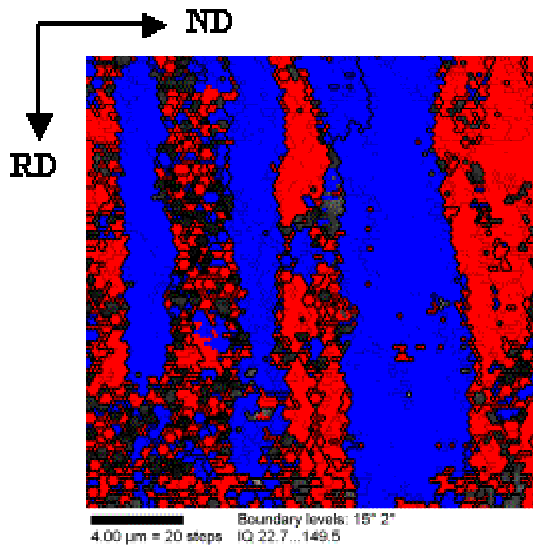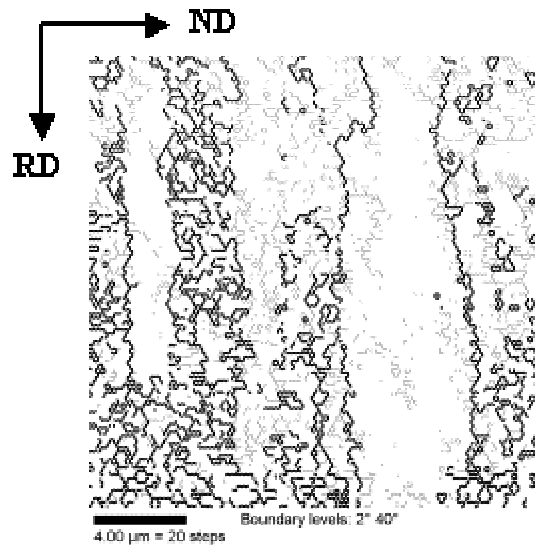
Figure 13.   OIM analysis of the AR16 as-received material. The pole figures (a) are highlighted to illustrate the texture variants which, when superimposed on the image quality grayscale map (b) clearly illustrates an alternating banded structure of texture variants. When the high angle grain boundaries (15º-65º) in (c) are accentuated (low angle boundaries, 2º-15º are in light gray), it becomes apparent that these banded structures are separated by high angle grain boundaries.

31

C. THE RECRYSTALLIZATION BEHAVIOR OF THE AR12 AND AR16 AA5083 ALLOY MATERIALS

Microstructural analysis of the annealed samples was conducted utilizing OIM to assess the extent of recrystallization as a function of annealing time at 450 ºC for the AR12 and AR16 materials. The annealing times were 0.1, 0.2, 0.5 and 1.0 hrs for both materials. The results of the AR12 samples are shown in Figure 14 as a series of image quality grayscale grain maps for each of the annealing times listed above. These data were obtained on a plane defined by the rolling direction and the thickness direction of the rolled sheet. Similar data was obtained for the AR16 material and is shown in Figure 15. The image quality grayscale grain maps for both materials reveal equiaxed grains that form within the first six minutes of annealing, with only slight grain growth occurring during annealing for times up to 1.0 hr. The texture data for both materials is shown in the form of discreet pole figures for each of the annealing times. The pole figures, for both the AR12 and AR16 materials, indicate that the B-type deformation texture of the as-rolled condition has been replaced by a nearly random texture within six minutes of annealing. The distribution of the grain-to-grain misorientation angles is also shown in Figures 14 and 15, for both materials at all annealing times. These distributions are almost identical to the Mackenzie distribution for randomly oriented cubes [Ref. 12] and are indicative of a fully recrystallized grain structure. Additionally, these materials are rich in high angle grain boundaries as indicated in Figure 16, where the image quality grayscale map for the AR16 material annealed for 1.0 hr has been re-plotted showing the grain boundaries with misorientations greater than or equal to 15º in heavy black lines and those with misorientations less than 15º in lighter black lines. The data for the AR12 material is essentially the same, and is not shown here. The image clearly shows that boundaries with misorientations greater than or equal to 15º surround the equiaxed grains in the material.

A plot of the area weighted average grain diameter as a function of annealing time (at 450 ºC) for both the AR12 and AR16 samples is shown in Figure 17. Again, these data suggest that the ARCO material is essentially recrystallized at 0.1 hr annealing time for either of the materials. The grain size of the more severely deformed material (AR12)

is finer than the less severely deformed material (AR16) at all annealing times. Grain growth rates have leveled off for both materials by one hour, consistent with the site-saturated model for recrystallization [Ref. 17]. Altogether, the microstructure and microtexture data are consistent with particle-stimulated nucleation (PSN) of recrystallization during heating after deformation processing [Ref. 5]. Additionally, this data suggests that this material meets the requirements for superplasticity; a fine, equiaxed grain structure with grain boundaries capable of supporting grain boundary sliding [Ref. 1].

The area weighted average grain diameter data for the AA5083 aluminum alloy 978901 and 978083 materials is included on the plot in order to compare the average grain size of the previously studied superplastically processed AA5083 aluminum alloy to the current alloy under study under a varying strain (%CW). Table 4 lists the area weighted average grain diameters and their corresponding percent reduction (%CW) for both alloys annealed at 450 ℃ for 1.0 hr. The grain size clearly decreases with increasing %CW. These data do not cover a sufficient range of reduction to assess the relationship between grain size and %CW.

Lot No.	$\bar{d}$ (μm)	% CW
978083	7.0	74.0
978901	7.4	74.0
AR12	7.7	76.0
AR16	8.7	66.0

Table 4.   Area weighted average grain diameter and %CW for all AA5083 aluminum alloys studied annealed at 450℃ for 1.0hr.
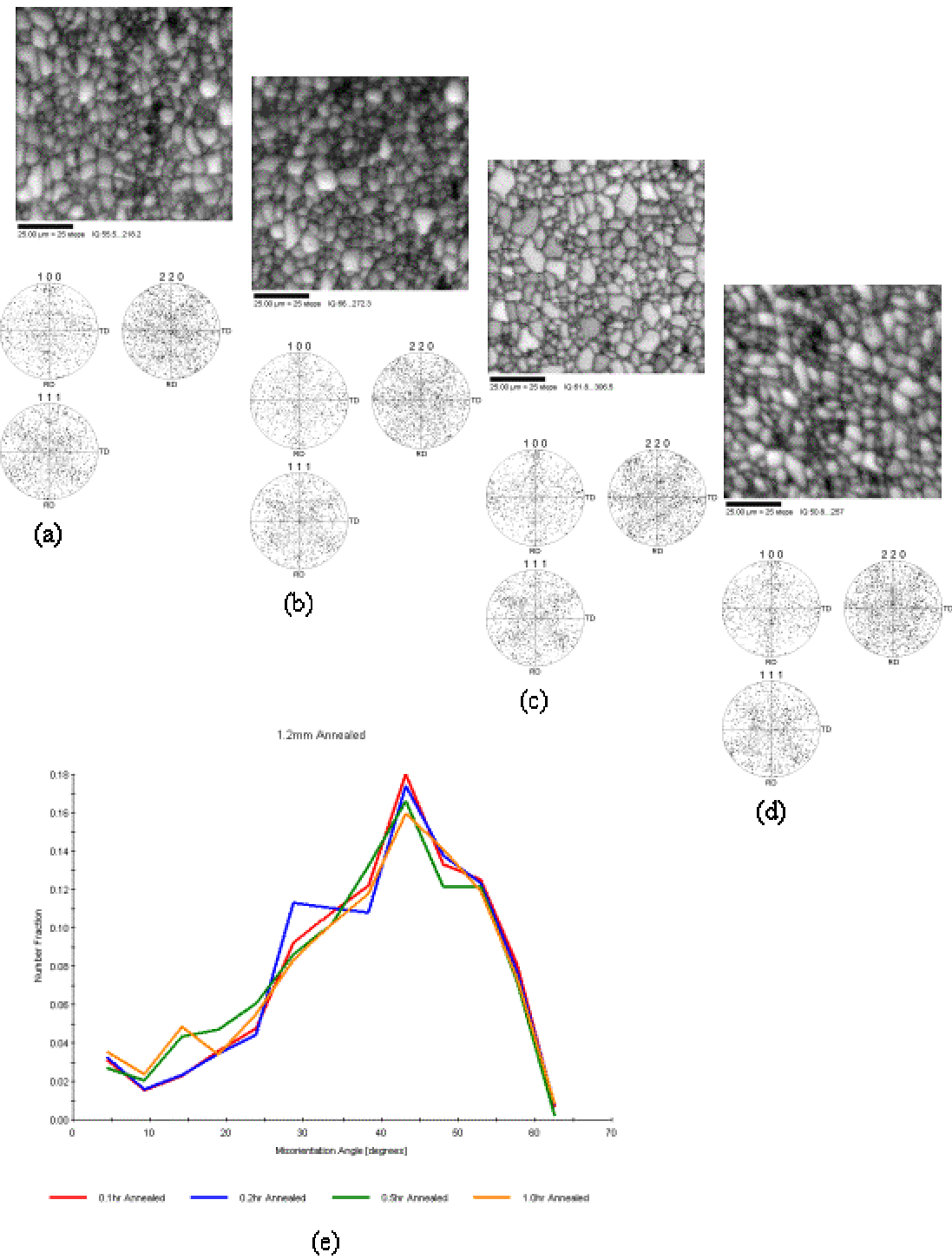
Figure 14.   OIM image quality grayscale maps and pole figures for the AR12 material for annealing times of (a) 0.1hr, (b) 0.2hr, (c) 0.5hr and (d) 1.0hr. The combined misorientation distribution for all annealing times reveals a Mackenzie like distribution indicative of a random orientation distribution consistent with a recrystallized structure.
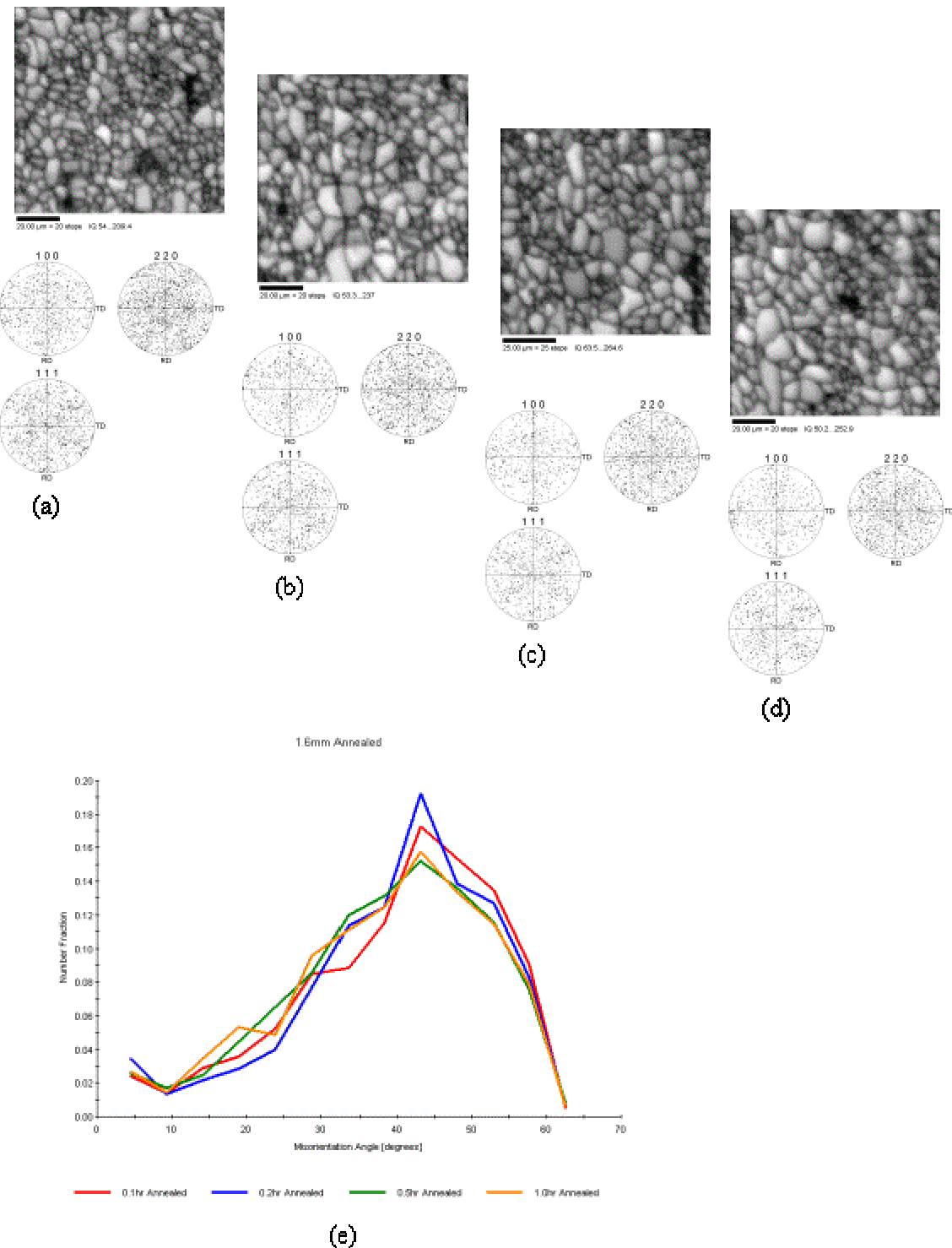
Figure 15.   OIM image quality grayscale maps and pole figures for the AR16 material annealed at 450ºC for (a) 0.1hr, (b) 0.2hr, (c) 0.5hr and (d) 1.0hr. The combined misorientation distribution diagram (e) suggests a Mackenzie like distribution indicating a random grain orientation distribution and a recrystallized structure.
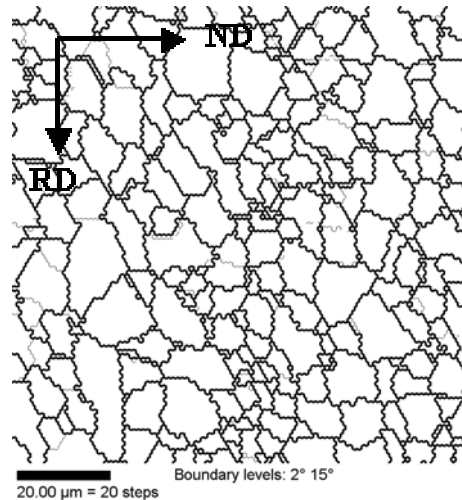
Figure 16.   Image quality grayscale grain map of the AR16 material after annealing at 450 ºC for 1.0hr highlighting grain boundaries with misorientation angles ≥15º in bold black lines and those with grain boundaries <15º in lighter black lines. The equiaxed grains are separated entirely by high angle grain boundaries.
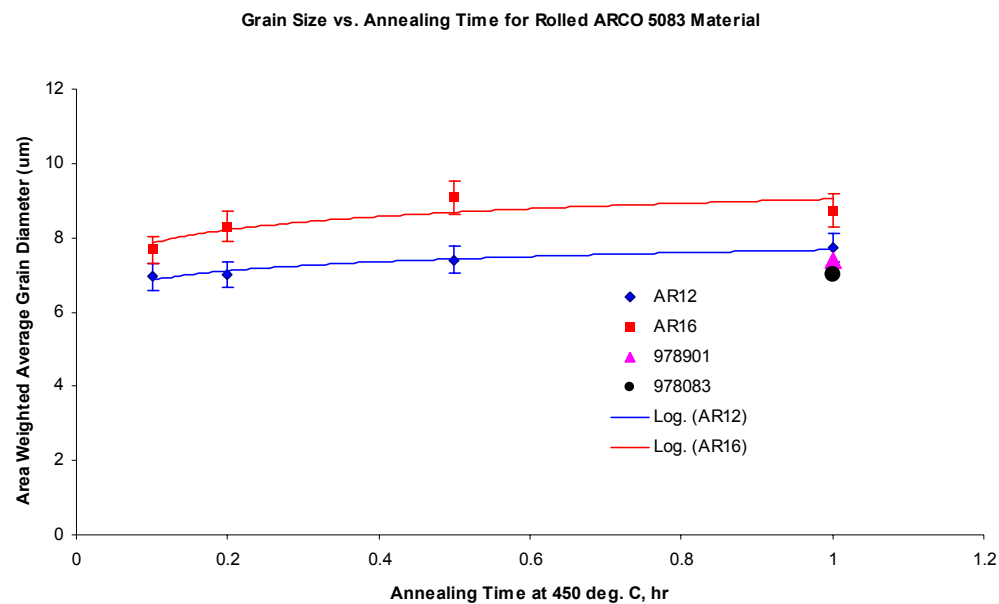
Figure 17.   The area weighted average grain diameter as a function of annealing time (at 450ºC) for the AR12 and AR16 materials. At all annealing times the material having the greater rolling reduction exhibits a finer grain size.

D.   MECHANICAL TESTING OF THE AA5083 ARCO MATERIALS

Elongation-to-failure (EF) tests were conducted at various strain rates, at a temperature of 450 ºC, on the ARCO materials. All the testing and analysis, summarized below, was performed by Taleff and Kulas, at the University of Texas at Austin [Ref. 15]. The test results are listed in Table 5. Included in the table is a quantitative measure of the degree of neck development at fracture. This parameter, q, is determined from the width, w, and the thickness, t, at the failure location of each sample; q is defined as follows, where A_0 is the cross-sectional area of the undeformed sample and $A = w \times t$ [Ref. 15]:

$$q = \frac{A_0 - A}{A_0}$$

The measure of neck development is made by comparing the measure q with the theoretical reduction-in-area, q^*, for a neck-free sample having the same elongation-to-failure, e_f, as that measured for the tested sample; q^* is defined as follows:

$$q^* = \left(1 - \frac{1}{1+e_f}\right) \times 100\%$$

A quantitative measure of necking, Q, is the normalized difference between q and q^*:

$$Q = \left(\frac{q - q^*}{q^*}\right) \times 100\%$$

Since the mode of failure for the AA5083 materials either by necking, cavitation, or a combination of the two, having a quantitative description of the degree of necking is beneficial [Ref. 15].

Additionally, elongation-to-failure tests were conducted on the 978083 and 978901 materials at a strain rate of $3 \times 10^{-4} s^{-1}$ for comparison with the ARCO materials, and, these results are included in Table 5.

Strain Rate (s^{-1})	Sample	e_f	q	q^*	Q (%)
3x10^{-2}	AR16A9	156	77.7	60.9	27.6
3x10-3	AR16A4	156	68.5	60.9	12.6
1x10-3	AR16A5	150	66.5	60.0	10.9
3x10^{-4}	AR16A6	153	65.8	60.4	9.0
3x10-2	AR12A9	171	76.3	63.0	21.1
3x10-3	AR12A2	165	70.8	62.3	13.6
1x10-3	AR12A3	150	67.0	60.0	11.6
3x10-4	AR12A4	160	68.5	61.5	11.3
3x10^{-4}	978083A25	204	74.9	67.1	11.7
3x10^{-4}	978901A20	179	66.9	64.1	4.3

Table 5. The values of e_f, q, q^*, and Q obtained at 450 ºC for three different types of materials at two different strain rates. (From: [Ref.15])

Additionally, e_f, Q and the stress exponent, n ($\equiv \frac{1}{m}$), were plotted for these materials as a function of strain rate [Ref. 15] and the results are shown in Figure 18. The data illustrates an increase in Q and n with increasing strain rate, which indicates an increase in necking with an increasing strain rate. However, e_f is constant at about 150% across this range of strain rate for the ARCO materials. This suggests that an increase in cavitation at lower strain rates offsets any beneficial effects of reduced necking, in the ARCO materials [Ref. 15].
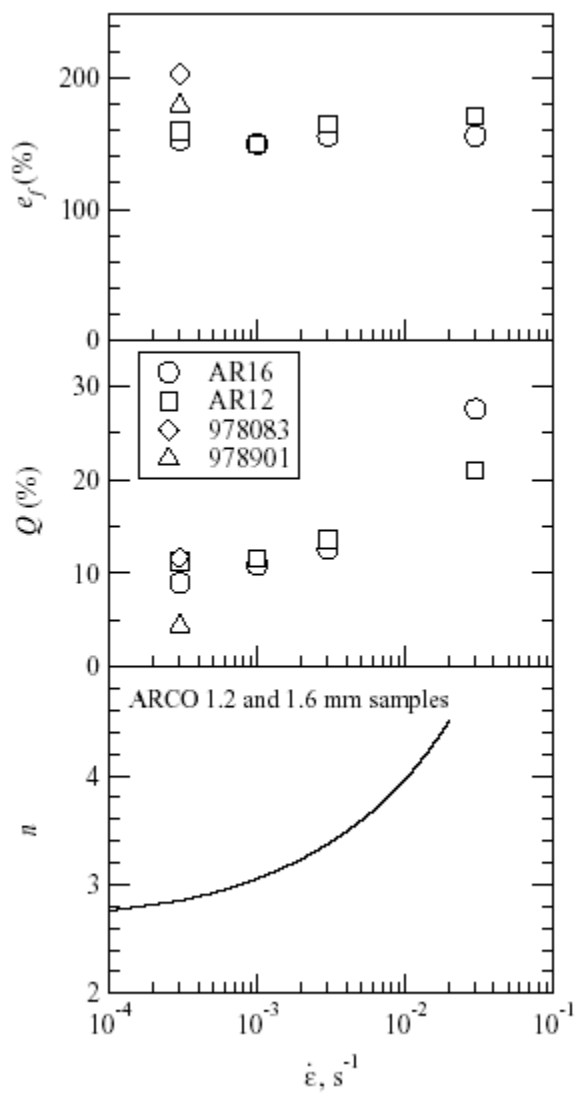
Figure 18.   Values of the stress exponent, n $(\equiv \frac{1}{m})$, of the ARCO materials (bottom), Q values for the ARCO and previously evaluated AA5083 materials (middle), and e_f of these materials (top) obtained at 450 ºC are plotted as functions of strain rate, $\dot{\varepsilon}$. High values of Q indicate strong neck development at the point of failure.

E.   MICROTEXTURE ANALYSIS OF THE AA5083 ARCO MATERIALS AS A FUNCTION OF STRAIN RATE

A microstructure and microtexture examination of the ARCO materials as a function of strain rate was conducted utilizing the OIM analysis software. The image quality grayscale grain maps of the AR16 material, with their corresponding pole figures are shown in Figures 19 and 20. The first grain map and pole figure combination, shown in Figure 19, is for material strained to failure at a strain rate of $3x10^{-4}$ s^{-1}. The microstructure, Figure 19(a), reveals some grain elongation in the RD. The corresponding pole figures, Figure 19(b), reveal a nearly random orientation distribution. It is also important to note the apparent formation of cavities, which may be identified in the IQ grayscale grain map, by the extremely dark regions corresponding to a very low IQ. The data shown in Figure 19 suggests that GBS is the dominant mechanism involved here.

The IQ grayscale grain map and pole figure data for this material deformed at a strain rate of $3x10^{-2}$ s^{-1} is shown in Figure 20. The microstructure, Figure 20(a), in this grain map reveals apparent grain size refinement as well as elongation in the rolling direction. The image quality is lower throughout the map, which is indicated by the greater number of grains with a darker appearance, in comparison to the data of Figure 19(a). This suggests greater strain energy is present in the structure, possibly due to an increased dislocation density and (sub) grain formation within the larger grains. Again, there also appears to be some cavity formation.

The microtexture data, as shown in the pole figures, Figure 20(b), at this strain rate, reveals a distinct deformation texture that is consistent with dislocation creep during tensile deformation. There appear to be two components in the deformation texture. The first component is a weak {001}<100> cube texture which is evident in the concentration of orientations along the RD, TD and possibly at the center of the {100} pole figure. The second component, a <111> fiber orientation, is readily apparent in the concentration of orientations along the RD in the {111} pole figure and as bands approximately 35º and 90º from the RD in the {220} pole figure. The observation of a definite fiber texture in these pole figures at a $\dot{\varepsilon} = 3 \times 10^{-2} s^{-1}$ is indicative of a dislocation creep dominated

mechanism and is consistent with previous studies on aluminum at this strain rate [Refs. 2, 5].

The misorientation distribution for three separate OIM scans for materials deformed at each strain rate is shown in Figure 21. At the strain rate in the GBS regime ($3x10^{-4}$ s^{-1}), the curves resemble a Mackenzie-like random distribution dominated by high angle boundaries, although there is a larger number fraction of low angle boundaries relative to the fully recrystallized AR16 misorientation distribution shown in Figure 14. For the strain rate in the dislocation creep regime ($3x10^{-2}$ s^{-1}) a much larger number fraction of low angle boundaries (2º-15º) reflect the possible formation of a substructure suggested by the lower image quality in the corresponding IQ grayscale grain map in Figure 20.

Finally, a microtexture analysis of the ARCO materials as a function of strain and strain rate during tensile deformation at 450 ºC is summarized in Figure 22. The mechanical testing data in Figure 22(a) was provided by Taleff and Kulas, at the University of Texas at Austin [Ref. 15]. The dashed lines in Figure 22(a) illustrate the regions where the strain rate is dominated by either GBS or dislocation creep. Figure 22 (b) and (c) are IQ grayscale maps that have been highlighted to show grain boundaries with grain-to-grain misorientations ≥15º in bold black lines and grain boundaries with grain-to-grain misorientations <15º with softer black lines. Figure 22(b) corresponds to a strain rate of $3x10^{-2}$ s^{-1}, and reveals a microstructure with a large number of low angle grain boundaries that appear to be directed in a transverse fashion with respect to RD. Figure 22(c) corresponds to a strain rate of $3x10^{-4}$s^{-1}, and reveals an equiaxed grain structure, slightly elongated in the RD, that is dominated by high angle grain boundaries. The results clearly show the change in microstructure as a function of strain rate during tensile deformation at 450 ºC. Also, the microtexture data for each strain rate, as indicated by the inset pole figures, is an indication of the straining conditions. The two dominant deformation mechanisms are clearly delineated, with the GBS regime characterized by a texture randomization and the dislocation creep dominated regime characterized by a fiber texture formation.
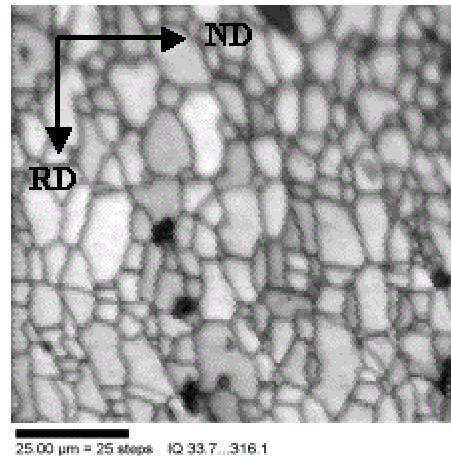
(a)
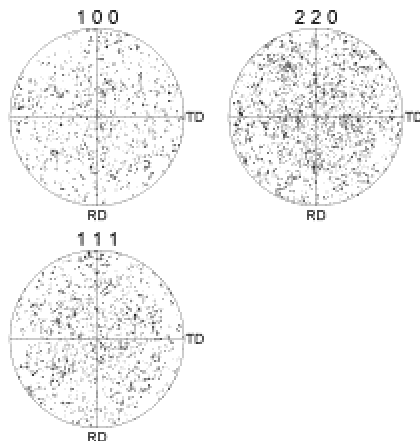
(b)

Figure 19.   Image quality grayscale grain map for material deformed at a strain rate of $3x10^{-4}$ s^{-1} (a), illustrating a equiaxed microstructure with a slight elongation of the grains in the RD. There is also an indication of cavities initiating at several sites between grains as indicated by the darker regions of lower IQ in the grain map. The pole figures (b) show a nearly random grain orientation. This microstructure/microtexture combination is consistent with that of a GBS dominated strain mechanism.

(a)

100   220

{001}<100>

Texture

111

<111> Fiber
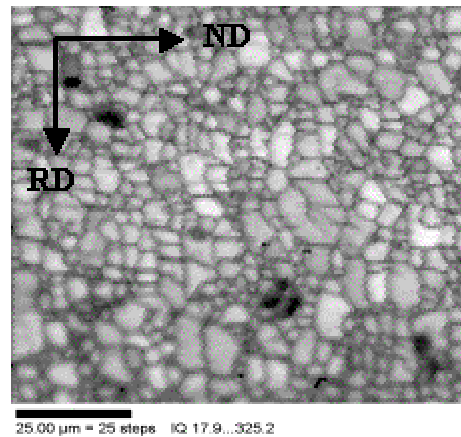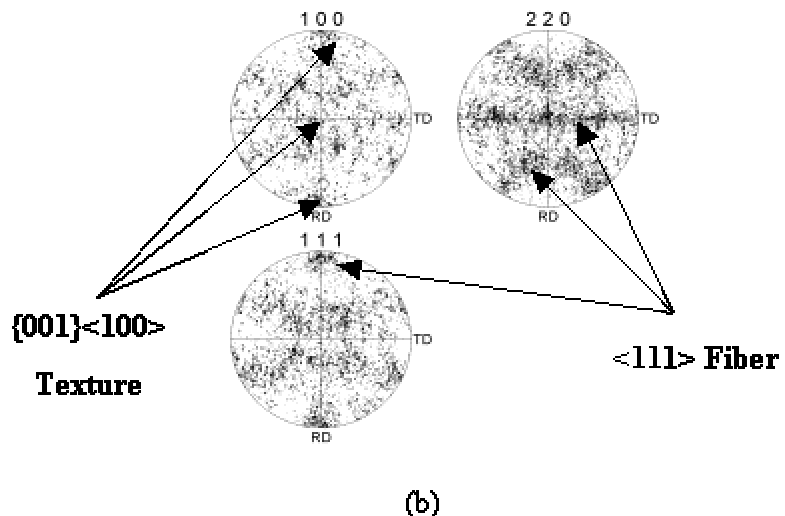
(b)

Figure 20.   Image quality grayscale grain map for material deformed at a strain rate of 3×10^{-2} s^{-1} (a), showing the microstructure. The grains appear smaller with a lower IQ overall indicative of a high strain energy condition. The microtexture is revealed using discreet pole figures (b). A definite deformation texture is present, with a distinct <111> fiber evident on the {220} pole figure and a faint {001}<100> texture component forming as shown in the {100} pole figure. This deformation texture is consistent with the type of microtexture seen for a dislocation creep controlled strain mechanism.
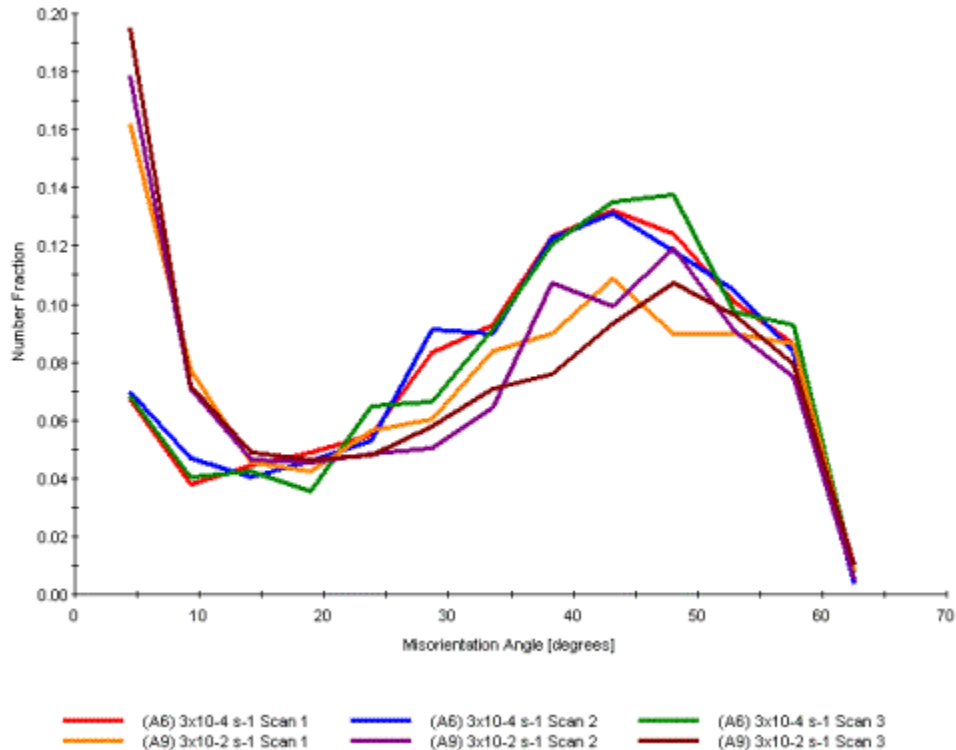
Figure 21. A combined grain-to-grain misorientation distribution for both strain rates of $3x10^{-4}$ s^{-1} and $3x10^{-2}$ s^{-1} showing three cases of each strain rate. The lower strain rate has a misorientation distribution resembling that of a Mackenzie random cube distribution, although there appears to be a slightly larger number fraction of grain-to-grain misorientations <15º, and is consistent with a GBS dominated strain mechanism. The higher strain rate has a misorientation distribution that is rich in grain-to-grain misorientations <15º, indicative of a (sub) grain structure forming. This is consistent with a dislocation creep dominated strain mechanism.
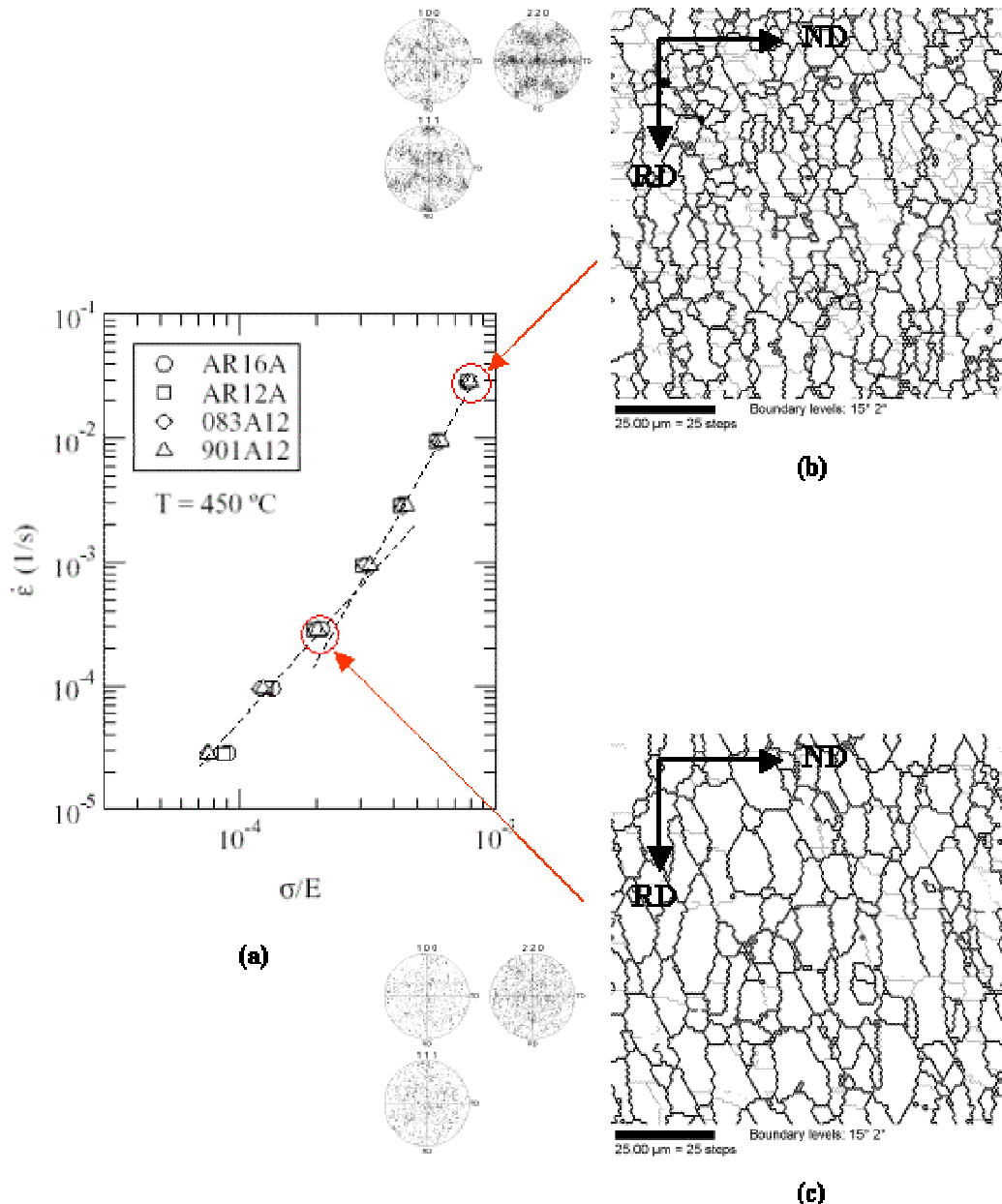
Figure 22.   Summary of microstructure and microtexture data for the AR16 material combined with the corresponding mechanical testing data for two strain rates consistent with GBS and dislocation creep dominated deformation. A strain rate of $3x10^{-2}$ s^{-1} (b) results in highly elongated, relatively smaller grains with a significant amount of low angle (<15º) grain boundary misorientations forming a (sub) grain structure. A strain rate of $3x10^{-4}$ s^{-1} (c) results in equiaxed grains slightly elongated in the RD, dominated by high angle (≥15º) grain boundary misorientations. (Mechanical data courtesy of Tulaff and Kulas [Ref 15]).

F.   THE STUDY OF CAVITY FORMATION IN AA5083 ALLUMINUM ALLOYS.

The OIM analysis of the microstructure and microtexture of the ARCO materials generated results that are consistent with previous studies conducted on AA5083 alloys. The ARCO material, designated AR12, that had been cold rolled to 76% reduction revealed a slightly finer grain size (~7 μm) with respect to the material that experienced a smaller reduction, designated AR16.   The AR16 material was cold rolled to 66% reduction and had a corresponding average grain size of ~8 μm.   The microtexture, following tensile deformation was consistent with that expected for the two strain rates studied. As a result of this, the ductility values of the ARCO materials were expected to be consistent with the values obtained for similar alloys deformed at 500 ºC. However, ductility values for the ARCO materials were significantly less than previously obtained. A comparison of all the ductility values for the ARCO materials and corresponding AA5083 materials, designated lot numbers 978083(A25) and 978901(A20), that were deformed under tensile conditions at 450 ºC are shown in Table 5 (Section IV-D) and a portion of that table is reproduced here for select materials, for review.

Material Designation	% Elongation to Failure (ε_f)
AR16(A9)	156
AR16(A6)	153
978901(A20)	178.5
978083(A25)	203.5
978901(A17) (Deformed at 500 ºC)	183
978083(A24) (Deformed at 500 ºC)	205

Table 6.   The mechanical testing data for selected materials investigated for cavitation behavior. (Mechanical data from Taleff and Kulas, [Ref. 15])

The Q values identified for these materials (see Table 5 Section IV-D) suggested that cavitation had played a role in the premature failure of these materials. An OIM analysis was conducted to identify the onset of cavitation in these materials and attempt to characterize the extent of cavity formation and the nature of the boundaries that had developed cavities.

The first of the materials examined by the OIM system were the AA5083 alloys deformed at 500ºC and $3\text{x}10^{-4}\text{s}^{-1}$ and designated lot numbers 978083(A24) or 978901(A17). The procedure used to identify the onset of cavitation involved stepping down the gage section of the tensile sample, scanning 100 μm^2 areas at each point, until the failure point was reached. Figure 23 illustrates how this was accomplished for the 978083(A24) material. Data was collected at each area scanned and displayed in the form of an image quality grayscale map. In each grayscale map, areas with low image quality will appear darker than the areas with a higher image quality; thus cavities will appear darker in these type of grain maps due to the low image quality at these points. The low image quality at the cavity site is due to the diffuse nature (or absence of) the diffraction patterns at this point. Therefore, a cavity can be defined, with respect to the OIM system, as a point in the area scanned with a significantly lower image quality relative to the surrounding points.

The cavities were than highlighted using a feature in the OIM analysis software that allows explicit areas to be highlighted based on a specific attribute. The attribute utilized here was image quality. The fact that the image quality of the areas presumed to be cavities was significantly lower than the surrounding areas allowed the OIM analysis software to differentiate them quantitatively. A histogram was generated for each 100 μm^2 area of the number fraction of points in the area as a function of image quality with the number of bins determined by Sturgis' Rule [Ref. 16]. The highlight feature was utilized to select, by bin, the area in the image quality grayscale map that corresponded, (in image quality), to that bin. When all the cavities were highlighted in the image quality grayscale map, the number fraction of all areas corresponding to cavities was summed resulting in the number fraction of points in the grayscale map that corresponded to cavities. This essentially resulted in an area fraction of cavities since a point in all the

image quality grayscale maps are identical in area. This same procedure was repeated at each area selected for analysis stepping down the gage section until the failure site was reached.

The data obtained for the materials designated 978083(A24) and 978901(A17) were collected in this fashion, with a total of eleven sites selected for analysis at approximately the same locations relative to the grip section on each sample. The total area scanned was 0.11 cm^2 over the length of each sample. Results are summarized in Table 7. Clearly, the material with the lower ductility (978901), wherein $\varepsilon_f = 183\%$, had a higher number fraction of cavities, approximately 3 times greater than the material of higher ductility (978083).

The 978901(A20) and 978083(A25) materials deformed at a temperature of 450 ºC were also analyzed using the same procedure at the same relative locations from the grip section. The results are also included in Table 7. Again, the material designated 978901(A20), where $\varepsilon_f = 178.5\%$, had a number fraction of cavities 2.7 times greater than the higher ductility material, 978083(A25) ($\varepsilon_f = 203.5\%$). It is noteworthy that the overall cavity volume fraction is higher at the higher deformation temperature. Also, it is important to note that the total area scanned for the materials deformed at 450ºC was less than for the materials deformed at 500 ºC.

Because the grain sizes and other features of these materials are essentially identical, this cavitation study suggests a direct relationship between the area fraction of cavities and the ductility of a material. Further analysis, however, is necessary to confirm these results.

The final step in the cavitation study was to characterize the nature of the boundaries that had sustained cavity formation. To this end, another feature of the OIM system was utilized that allows the user to identify the misorientation angle between any two points on a grain map. In order to identify the type of misorientation that existed prior to cavity formation, the same image quality grayscale grain maps were utilized, wherein the cavities are defined as in the previous analysis. The analysis of the 978901(A17) material resulted in 101 different misorientations. A histogram showing

the distribution of the range of misorientations by number is shown in Figure 24, for this material. The data shows cavity formation for misorientation angles $\geq 7°$. The data for the 978083(A24) material is shown in Figure 25 as a distribution histogram. The data set for this material is half that of the 978901(A17) material ($N = 50$) due to the smaller number fraction of cavities present in this material. However, this data suggests that boundaries with misorientations $\geq\approx 10°$ are the type of boundaries most likely to develop a cavity.

The shape of the distribution in Figure 24 is similar to the Mackenzie distribution above about 10°. Since the distribution in the annealed, undeformed condition was essentially the Mackenzie random distribution, it can be concluded that boundaries above about 10° misorientation have a probability of separation in approximate proportion to the relative number of such boundaries in the microstructure.

Material Designation	450ºC		500ºC	
	Cavity Number Fraction	ε_f (%)	Cavity Number Fraction	ε_f (%)
978083	0.00635	204	0.01348	205*
978901	0.01715	178	0.04104	183

* Did not fail.

Table 7.   The number fraction of cavities and % elongation to failure for the AA5083 alloys deformed at elevated temperatures of 450ºC and 500ºC.
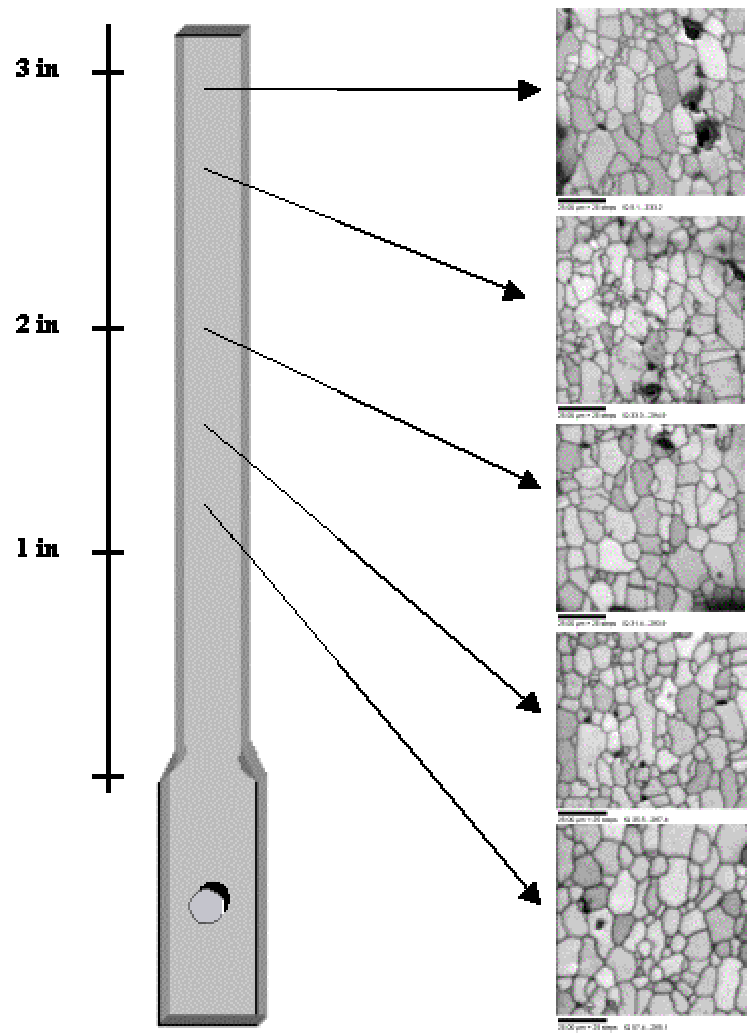
Figure 23.   An illustration of the method used to "step down" the gage section of the sample. The image quality grayscale maps are from the material designated 978083(A24), deformed at 500 ºC and are typical of all the data taken for the other materials. The relative locations, examined by the OIM system, are similar on the other samples.
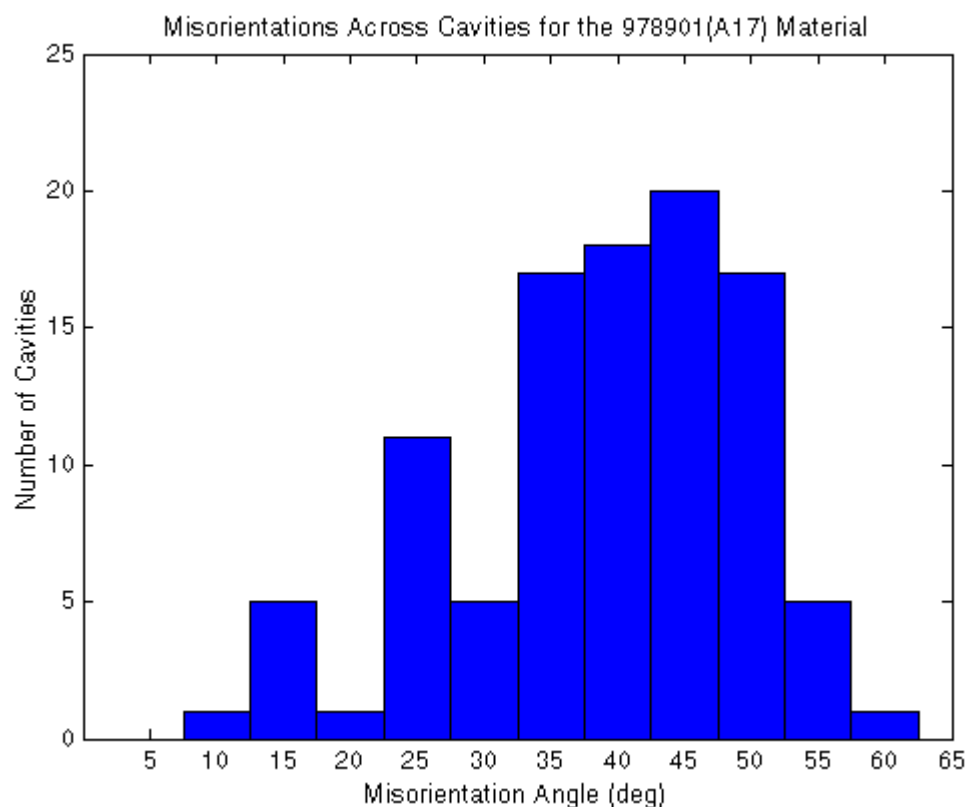
Figure 24.   Histogram showing the distribution of cavities as a function of misorientation angle for the 978901(A17) material deformed at 500 ºC.
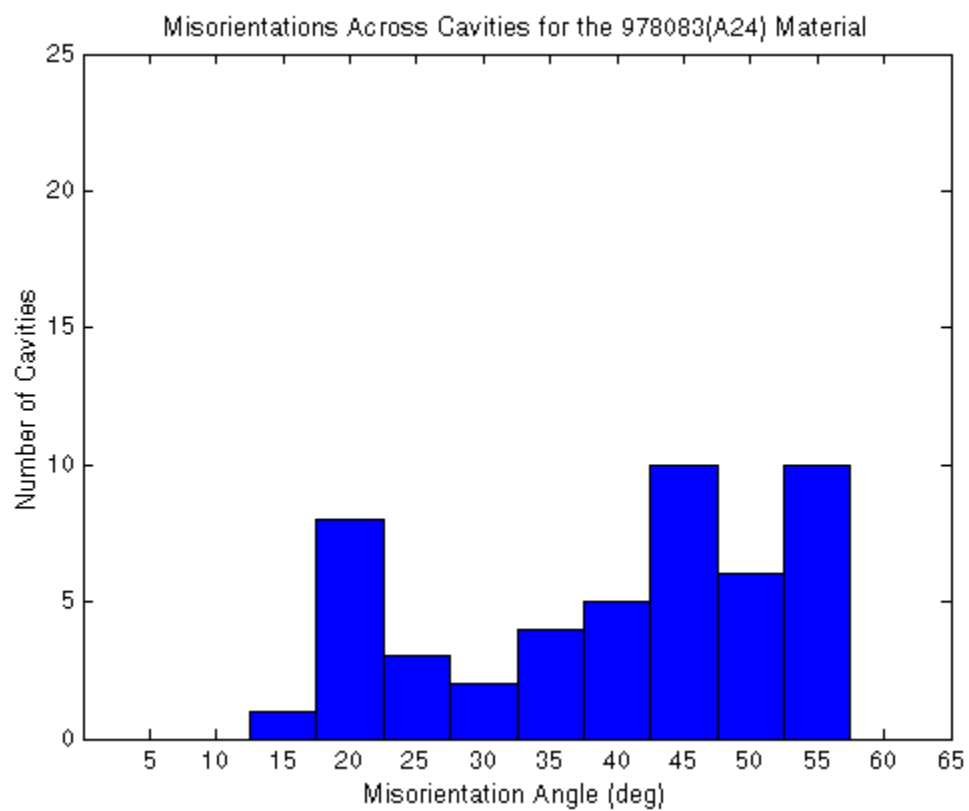
Figure 25.   Histogram showing the distribution of cavities as a function of misorientation angle for the 978083(A24) material deformed at 500 ºC. Note the data set is smaller due to the smaller number fraction of cavities.

V   CONCLUSIONS

A.   CONCLUSIONS

1. The hot-band ARCO material revealed an annealed microstructure and finer grains than expected. The microtexture data revealed a weak cube component in an otherwise random texture. The grain boundary misorientation distribution was random in nature.

2. The ARCO sheet material was in a cold rolled condition. The microstructure revealed grains highly elongated in the RD. The microtexture consisted of a B-type deformation texture and an alternating layered structure of bands having lattice orientations corresponding to the variants of the B-texture component.

3. Annealing of two ARCO materials, cold rolled to different reductions, was conducted to determine the recrystallization behavior as a function of time at 450ºC. The microstructure of both materials revealed fine, equiaxed grains at six minutes annealing time, and all subsequent times (0.2hr, 0.5hr and 1.0hr). The area weighted average grain size for the materials at 1.0 hr annealing at 450ºC was ~7 μm (76% CW) and ~8 μm (66% CW), with only slight grain growth after 0.1 hr annealing. The microtexture revealed a random texture for all annealing times. The ARCO material tested was essentially recrystallized after 6 min annealing at 450ºC.

4. Microstructure and microtexture analysis of the ARCO materials strained at strain rates corresponding to the GBS dominated and dislocation creep dominated regimes resulted in data consistent with previous studies.

   a. A clear deformation texture existed for a strain rate in the dislocation creep regime, with a microstructure consisting of fine (sub) grains within larger elongated grains, surrounded by high angle boundaries

b. A random texture with slight elongation in the direction of applied stress was evident for the strain rate corresponding to the GBS dominated regime.

5. Mechanical data revealed ductility data for the ARCO material and additional AA5083 alloys deformed at 450ºC to be significantly less than expected for the grain size achieved by processing.

6. A cavitation study was conducted on two AA5083 materials deformed at 500ºC and 450ºC, which suggests that low ductility values correlated with the number fraction of cavities formed. Additionally, the data suggests that boundaries with higher misorientations are the type of boundaries most likely to form a cavity.

B.   RECOMMENDATIONS FOR FURTHER STUDY

1. Continued analysis of the cavitation behavior of these superplastic aluminum alloys as a function of strain, strain rate and temperature.

2. Further study of the ARCO hot-band materials.

3. Application of OIM to a component undergoing superplastic forming to determine local deformation mechanisms.

4. Application of OIM and microtexture analysis to a wider range of superplastic materials, processing conditions and microstructures.

THIS PAGE INTENTIONALLY LEFT BLANK

LIST OF REFERENCES

1   Nieh, T.G., Wadsworth, J., and Sherby, O.D., *Superplasticity in Metals and Ceramics*. Cambridge University Press, New York, 1997.

2.   Harrell, J.W., *Analysis of the Transition in Deformation Mechanisms in Superplastic 5083 Aluminum Alloys by Orientation Imaging Microscopy*, Master's Thesis, Naval Postgraduate School, Monterey, CA, September 2001

3.   McNelley, T.R, and McMahon, M.E., *Journal Of Metals,* v. 48, 2, 1996.

4.   McNelley, T.R., McMahon, M.E., and Hales, S.J., *Scripta Materiallia,* v .36, p.369, 1997.

5.   Pérez-Prado, M.T., González-Doncel, G., Ruano, O.A., and McNelley, T.R., *Acta Materialia*, v. 49, p. 2259, 2001.

6.   Ruano, O. A., Miller, A. K., and Sherby, O.D., *Mater. Sci. Eng.*, v. 51, p.9, 1981.

7.   Sherby, O.D. and Ruano, O.A., *Superplastic Forming of Structural Alloys*, ed. N.E. Patton and C. H. Hamilton, TMS-AIME, New York, 1982, p241.

8.   Kokawa, H., Watanabe, T., and Karashima, S., *Phil. Mag. A*, v. 44, p. 1239, 1981.

9.   Randle, V., *Microtexture Determination and Its Applications,* The Institute of Materials, 1992.

10. Krajewski, P.E., Private Communication, March, 2002.

11. Bunge, H.J., *Texture Analysis in Materials Science*, Butterworths, 1982.

12. Mackenzie, J.K., *Biometrica*, v.45, p.229, 1958.

13. Swisher, D.L., *Production of Ultra-Fine Grains and Evolution of Grain Boundaries During Sever Plastic Deformation of Aluminum and it Alloys*, Master's Thesis, Naval Postgraduate School, Monterey, CA, December 2000.

14. Doherty, R. D., Hughes, D. A., Humphreys, F.J., Jonas, J.J., Juul Jenson, D., Kassner, M. E., King, W. E., McNelly, T. R., McQueen, H. J. and Rollett, A. D., *Mater. Sci. Eng.,* v. A238, p. 219, 1997.

15. Taleff, E.F. and Kulas, M. A., Private Communication, February, 2002.

16.   Beckwith, T.G., Marangoni, R.D., Lienhard V., J.H., *Mechanical Measurements*. 5TH ed. Addison-Wesley Publishing Company, Inc., New York, 1993.

17.   Shewmon, P.G., *Transformations in Metals*. McGraw-Hill, 1969

INITIAL DISTRIBUTION LIST

1.   Defense Technical Information Center
        Ft. Belvoir, Virginia

2.   Dudley Knox Library
        Naval Postgraduate School
        Monterey, California

3.   Engineering and Technology Curricular Office, Code 34
        Naval Postgraduate School
        Monterey, CA

4.   Department Chairman, Code ME/Mc
        Naval Postgraduate School
        Monterey, CA

5.   Professor Terry R. McNelley, Code ME/Mc
        Naval Postgraduate School
        Monterey, CA

6.   Professor Eric Taleff
        The University of Texas at Austin
        Austin, TX

7.   Dr. Paul E. Krajewski
        General Motors Corp.
        Warren, MI

8.   LT. Tracy A. Maestas
        Naval Postgraduate School
        Monterey, CA